PUBLICATIONS OF THE ASTRONOMICAL SOCIETY OF THE PACIFIC, **110**:339–364, 1998 March

A High-Altitude Site Survey for SOFIA

MICHAEL R. HAAS

MS 245-6, Space Science Division, NASA Ames Research Center, Moffett Field, CA 94035-1000; haas@cygnus.arc.nasa.gov

AND

LEONHARD PFISTER

MS 245-5, Earth Science Division, NASA Ames Research Center, Moffett Field, CA 94035-1000; pfister@telsci.arc.nasa.gov

Received 1996 December 16; accepted 1997 November 28

ABSTRACT. The Stratospheric Observatory for Infrared Astronomy (SOFIA) is a modified Boeing 747-SP equipped with a 2.5 m telescope dedicated to astronomical research. Currently under joint development by the US (NASA) and Germany (DLR), it is scheduled to begin operations in late 2001. The ability of SOFIA to carry out its mission will depend strongly on the meteorological conditions at and above flight altitudes in the vicinity of its home base. The most important meteorological factors are the frequency of high-altitude clouds and the magnitude of the water vapor overburdens. This paper performs a high-altitude site survey by gathering together the best available meteorological data, defining metrics, and evaluating them for a variety of sites. These metrics are found to corroborate past airborne experience and to be consistent with well-known global circulation patterns, convection, and upper tropospheric dynamics. They indicate that there are significant variations in the weather at SOFIA flight altitudes. Particularly in summer, some continental US sites are shown to be worse than Hawaii, where high-altitude cirrus clouds and the associated moisture have historically caused significant losses in the amount and quality of the astronomical data collected by NASA's Kuiper Airborne Observatory. SOFIA's planned home base, Moffett Field, CA, is found to have excellent high-altitude weather and to be one of the best continental US sites.

1. INTRODUCTION

Before any major new ground-based astronomical facility is developed, it is customary and appropriate to monitor proposed sites to assess their suitability and comprehend their limitations. Site surveys usually extend over several years and record such meteorological quantities as the annual precipitation, wind speed and direction, relative humidity, cloud cover, near-ground turbulence, and vertical structure and diurnal variations of temperature (see, e.g., Morrison et al. 1973; Erasmus 1986). In addition, some astronomically important quantities such as seeing, visible sky brightness, and infrared sky emissivity are often measured directly. Ultimately, such data are used to help select the site that best fulfills the scientific objectives of the facility under development.

In the case of airborne astronomy, the number of facilities has historically been very limited and will remain so for the foreseeable future. Most of the observations to date have been made with the 91 cm telescope of the recently retired Kuiper Airborne Observatory (KAO; Cameron, Bader, & Mobley 1971) or its predecessor, the 30 cm telescope of the Learjet Observatory (LJO; Bader & Wagoner 1970). Moreover, the bulk of the world's airborne astronomy has been conducted from the NASA Ames Research Center, Moffett Field, CA. Routine access to the southern skies has been provided by deployments, primarily to Hickam Field, HI, and Christchurch, New Zealand. These three sites were selected largely for programmatic reasons, with some considerations, mostly intuitive, given to local meteorological conditions.

Past experience indicates that the most important meteorological quantities affecting the quality of astronomical observations at flight levels between 41,000 and 45,000 feet (12.5–13.7 km) are high-altitude cloud cover and water vapor overburden. Recent satellite observations of the Earth's atmosphere have, for the first time, produced a meteorological database that includes global coverage of these quantities at the appropriate altitudes as a function of season—that is, data sets suitable for conducting a high-altitude site survey. This is an appropriate time to undertake such a study, as the Stratospheric Observatory for Infrared Astronomy (SOFIA; Erickson & Davidson 1995) has recently entered joint development by NASA (US effort) and DLR (German effort). This unique observatory is scheduled to be operational near the end of 2001. It will have a 2.5 m (effective aperture) telescope mounted in the aft section of a Boeing 747-SP for use in astronomical observations between 0.3 and 1600 μm. It has a planned operational lifetime of 20 years and a nominal flight rate of 160 flights yr^{-1}.

This paper shows that there are significant weather patterns

above SOFIA flight levels and, therefore, that selecting a suitable home base and identifying acceptable deployment sites for operations can play a major role in maximizing SOFIA's scientific productivity. The effects of high-altitude clouds on airborne astronomy and their frequency of occurrence as a function of season and geographic location are presented in § 2. The impact of the water vapor overburden and estimates of its variation with season and geographic location are given in § 3. These meteorological data are discussed in the context of our general understanding of global circulation and other well-known meteorological phenomena in § 4. Metrics are proposed, evaluated, and intercompared in § 5 for those sites that have been used for extensive KAO operations, those considered for SOFIA operations, and other geographically distributed sites. The results are discussed and briefly summarized in § 6.

2. HIGH-ALTITUDE CLOUDS

2.1. The Effects of Clouds on Airborne Astronomy

High-altitude clouds are primarily composed of nonspherical ice crystals with effective sizes of 5–25 μm (Platt, Spinhirne, & Hart 1989; Spinhirne & Hart 1990). Consequently, their near-infrared ($\sim$10 μm) absorption coefficient is typically twice their visible extinction coefficient (Platt 1979; Platt et al. 1989; Wylie et al. 1995), and their optical depth decreases at longer wavelengths. The impact of such clouds on airborne astronomy depends on their properties and the nature of the investigation being conducted. If the clouds have significant optical depth, they modulate the infrared signal from the source in an indeterminate way and obscure the visible track and guide stars so that the telescope cannot be stabilized and/or pointed—no useful astronomy can be done under these observing conditions.

If the optical depth of the clouds is small, their major effect is to add excess "sky noise" (Tarrius, Papoular, & Lebertre 1982), since they radiate in the infrared at a substantially warmer temperature than space. Such extraneous noise is well known to ground-based infrared observers (see, e.g., Westphal, Neugebauer, & Leighton 1974) and is, unfortunately, also experienced by airborne observers (Wijnbergen, Léna, & Celnikier 1978). The impact of this cloud noise, N_c, can be estimated by comparing it to the photon noise, N_b, experienced for background-limited instrument performance (BLIP). Photon noise is the statistical fluctuation of the photon flux from a constant background (e.g., a perfectly still atmosphere or a constant-temperature telescope; Tarrius et al. 1982) and is given by

$$N_b = \sqrt{2u\tau_b\eta P_b t/h\nu}, \tag{1}$$

where u characterizes the noise generation in photovoltaic ($u = 1$) or photoconductive ($u = 2$) detectors, τ_b is the instrumental transmission for the background, η is the detector quantum efficiency, $h\nu$ is the photon energy, t is the observing time, and $P_b = \epsilon_b A\Omega\delta\lambda B_\lambda(T_b)$. The latter is the background power seen by an instrument with throughput $A\Omega$, spectral bandwidth $\delta\lambda$, and background emissivity ϵ_b. The quantity $B_\lambda(T_b)$ is the blackbody brightness function at wavelength λ for an effective background temperature T_b.

For typical air speeds and chopper (oscillating secondary mirror) frequencies ($\sim$10–30 Hz), the maximum effect occurs when the clouds vary on length scales of $\sim$10 m. If the clouds appear uniform over much larger distances, then their noise has the functional form in equation (1) and

$$\frac{N_c'}{N_b} = \sqrt{\frac{\epsilon_c B_\lambda(T_c)}{\epsilon_b B_\lambda(T_b)}}, \tag{2}$$

where T_c is the cloud temperature, ϵ_c is the cloud emissivity, and b again refers to the constant background seen by the detectors. Alternatively, if the optical depth of the clouds fluctuates significantly on small length scales, then the observed cloud power, P_c, is modulated directly by a factor $f \lesssim 1$, and the ratio of the cloud noise to BLIP is

$$\frac{N_c''}{N_b} = \frac{\tau_s\eta f P_c t}{\sqrt{2u\tau_b\eta P_b t/h\nu}} = \frac{f P_c\sqrt{t}}{\mathrm{NEP}}, \tag{3}$$

where $\tau_s = \tau_b$ times the telescope transmission is the signal transmission (including losses from obscuration, reflectance, diffraction, and chopper efficiency) and NEP is the system noise equivalent power for BLIP.

The noise ratio N_c'/N_b in equation (2) is independent of instrumental bandpass and is of order $\epsilon_c^{1/2}$ for typical KAO parameters and $\lesssim$2 times larger for SOFIA (because the telescope will have lower emissivity), so the cloud noise should never significantly exceed BLIP. Considerably larger noise excesses are predicted by equation (3), unless the variations in cloud optical depth are very small ($\tau_c \ll 0.01$) on the length scales of interest. Moreover, the ratio N_c''/N_b is proportional to the square root of the instrumental bandpass, so broadband instruments are more susceptible to variations in cloud optical depth than are narrowband instruments.

The latter behavior is consistent with cloud encounters on the KAO, where it was generally found that (1) broadband airborne instruments were more affected by clouds than narrowband instruments and (2) the excess noise produced by clouds sometimes exceeded BLIP by factors of $\sim$10 and, on occasion, factors of $\sim$100 or more (C. D. Dowell, private communication). Hence, at least some of the excess noise associated with clouds is from optical depth variations on the appropriate length scales. Nonetheless, photon noise should not be neglected, as it represents the minimum possible noise increase (e.g., for uniform clouds with an optical depth $\tau_c = 0.01$, eq. [2] gives $N_c/N_b \sim 0.1$, which translates into a 20% increase in observing time relative to cloud-free conditions).

Although it is well known that photometry is more affected by overlying clouds than is spectroscopy, as is the case for

ground-based astronomy (Hall 1968), the question of exactly which clouds impact which airborne observations is difficult to quantify. Here we adopt an empirical approach and simply intercompare the frequency of cloud occurrence at the various sites of interest and relate them to the KAO's observing experience. Since thin, transmissive cirrus are found in roughly half of all satellite observations, good vertical resolution is essential to assess their effects on airborne astronomy. The existing meteorological data sets that best measure high-altitude cloud cover are the satellite observations of SAGE II (Wang et al. 1996) and HIRS (Wylie et al. 1994).

2.2. The SAGE II Frequency of Cloud Occurrence

The Stratospheric Aerosol and Gas Experiment (SAGE II; McCormick et al. 1979; McCormick 1987) aboard the *Earth Radiation Budget Satellite* (*ERBS*) has used a limb occultation technique to monitor the cloud and water vapor content of the stratosphere and upper troposphere since 1984. The experiment recovers the extinction over a ~200 km horizontal path with good (~1 km) vertical resolution. Clouds are distinguished from aerosols using a variant of the two-wavelength method developed by Kent et al. (1993). Comparisons with lidar over the south Pacific suggest that SAGE II tends to underestimate the height of the clouds by assuming they are all at the tangent point (Kent et al. 1995).

Wang et al. (1996) have produced a 6 yr climatology from the SAGE II data and provide the frequency of occurrence for their "subvisual" ($0.0002 < \tau_{vis} < 0.02$) and "opaque" ($\tau_{vis} > 0.02$) clouds as a function of altitude, where τ_{vis} is the optical depth at 0.7 μm. In Figure 4 the probability of occurrence for the two cloud types has been combined and vertically integrated by P. M. McCormick et al. (private communication) to produce the total frequency of cloud occurrence, f_{SAGE}, above FL410 (flight level 41,000 feet or 12.5 km) for the four seasons (DJF, MAM, JJA, and SON). The geographic region displayed is 0°–60° north latitude and 40°–180° west longitude, which is referred to below as the North American Region. The SAGE II cloud climatology is remarkably consistent with cloud climatologies derived from other sources (Liao, Rossow, & Rind 1995; Wang et al. 1996).

2.3. The HIRS Frequency of Cloud Occurrence

Statistics on clouds have been compiled from High-Resolution Infrared Radiation Sounder (HIRS) sensors on polar orbiting NOAA satellites since 1989 June (Wylie et al. 1994). A description of the "CO_2 slicing algorithm" used to derive cloud altitudes from the 13–15 μm HIRS channels with partial CO_2 absorption is given by Wylie et al. (1994). The most recent data can be viewed on the World Wide Web at http://wylie.ssec.wisc.edu.

Since the satellite is nadir looking, this data set has much better horizontal resolution than SAGE II (§ 2.2). It is reported on a $2^\circ \times 3^\circ$ grid and represents the vertically integrated frequency of occurrence for clouds with visible optical depths greater than 0.3. These HIRS data are believed to provide a better means of deriving altitudes for semitransparent clouds than other nadir-viewing techniques. However, intercomparisons with lidar by Baum, Wielicki, & Minnis (1992) and Wylie & Menzel (1989) show that HIRS underestimates cloud top altitudes by about 1 km. This is consistent with the error analysis of Menzel, Wylie, & Strabala (1992), who find that nearly all sources of error tend to bias the clouds to lower altitudes. For this reason, Wylie has provided a "corrected" data set, in which the cloud altitudes have been raised by 1–2 km, depending on their optical depth (see the Wylie Web site above).

Given the uncertainty of these corrections, and the fact that they vary with the nature of the clouds (which may vary with location), only the "uncorrected" data are used here. Hence, these data are almost certainly a conservative estimate of the frequency of clouds having optical depths $\gtrsim 0.3$. The monthly data from 1989 June to 1995 November have been averaged for each season and interpolated to FL410 to give the frequency of cloud occurrence, f_{HIRS}, shown in Figure 5.

2.4. High-Altitude Cloud Cover (Normalization)

SAGE II and HIRS provide the frequency of occurrence, f_{SAGE} and f_{HIRS}, for high-altitude clouds with small and moderate optical depths, respectively. When clouds are present, the fractional cloud cover, f_{cover}, is the fractional surface area occupied by clouds (see Warren et al. 1986, p. 11). Also called the area filling factor, this quantity characterizes the cloud structure. By definition, $f_{cover} \leq 1$ and is used to derive the average total cloud cover, C, from the relationship

$$C_X = f_{cover} f_X, \tag{4}$$

where f_X (e.g., either f_{SAGE} or f_{HIRS}) is the frequency of cloud occurrence. Since f_{cover} is nearly independent of location (Warren et al. 1986), the relative merits of sites for airborne astronomy can be determined by direct comparison of f_X ratios. However, the actual values of total cloud cover are also of interest, as they represent the fraction of flight time spent in or under clouds and thereby set the scale of the problem. For example, if f_{cover} for high clouds were very small, say $\lesssim 0.01$, then the total cloud cover would be small even when the frequency of occurrence approached 100%, which implies minimal cloud impact at all sites.

The fractional cloud cover, f_{cover}, is estimated in two ways. First, for SAGE II, Liao et al. (1995) derive a simple formula for f_{cover} that is nearly linearly dependent on the assumed cloud size, l, and is fairly insensitive to F, the probability that a given cell along the SAGE II line of sight is occupied by a cloud. Liao et al.'s preferred normalization to the ISCCP data (Schiffer & Rossow 1983) finds $l = 75$ km and $F = 0.2$, which gives $f_{cover} = 0.45$. This value is consistent with the results of satellite measurements (see, e.g., Baum et al. 1995), which show that

when high-altitude cirrus clouds form, they usually extend over ~100 km distances. It is also fairly consistent with the average value of $f_{\rm cover} \sim 0.45$ for high clouds in a global climatology based on surface observations (Warren et al. 1986). This latter climatology also shows that the global variation in $f_{\rm cover}$ is small; most values cluster between 0.4 and 0.5 with extremes of about 0.3 and 0.6.

Second, the impact of clouds on airborne astronomy is assessed by examining flight records of KAO cloud encounters during deployments to Hawaii. Although this information is more subjective and anecdotal than the compiled cloud statistics, it provides a more direct estimate of what SOFIA may actually experience. Meyer (1996) finds that clouds were recorded on 44% of the 147 flights in Hawaii between 1978 and 1995 (i.e., $f_{\rm KAO} = 0.44$) and that the average cloud occurrence lasted 36 minutes. Since KAO flights typically had 390 minutes of observing time, this implies $f_{\rm cover} = 0.09$, resulting in $C_{\rm KAO} = 0.04$. Meyer surmises that these anecdotal records probably underestimate both the frequency and duration of the actual cloud events, so these values should be viewed as lower limits.

All of these flights occurred between May and September, and most of them (~3/4) occurred in the summer season (JJA). The KAO frequency of cloud encounters, $f_{\rm KAO}$, is comparable to the SAGE II results shown in Figure 4*c*. When averaged over a typical flight area in the vicinity of Hawaii (see § 5), the frequency of cloud occurrence above FL410 in the summer is $f_{\rm SAGE} = 0.33$. The SAGE II value for $f_{\rm cover}$ is uncertain but probably lies in the range $0.09 < f_{\rm cover} < 0.45$, as discussed above. The important point is that even the smallest of these values (an admitted lower limit) is significant, resulting in 3% cloud cover for Hawaii in the summer. Using the geometric mean of the above two extremes for $f_{\rm cover}$, the SAGE II estimate of cloud cover is

$$C_{\rm SAGE}(x, y) = 0.2 f_{\rm SAGE}(x, y). \quad (5)$$

This value of $f_{\rm cover}$ represents a reasonable compromise. It recognizes that the anecdotal KAO value is certainly an underestimate, whereas the Liao et al. and Warren et al. values for $f_{\rm cover}$ probably include some SAGE II clouds that are too thin to impact airborne observations. Because $f_{\rm KAO} \sim f_{\rm SAGE}$, the latter is used as an estimate of the fraction of full-length flights that will encounter at least one episode of clouds, and $C_{\rm SAGE}$ is used as an estimate of the fraction of total flight time spent in or under high-altitude clouds.

The HIRS cloud data can be renormalized to provide similar quantities, but the normalization constants are larger because the cloud frequencies reported by HIRS are substantially smaller than those for SAGE II. This is entirely expected, given that the HIRS observations have an optical depth cutoff of 0.3, while SAGE II presumably measures all clouds. The importance of the HIRS data, of course, is that they have significantly better horizontal resolution, thus locating the regions of high cloudiness more precisely. The fact that the same cloud patterns appear in both climatologies (see Figs. 4 and 5) suggests that the thin clouds measured by SAGE II are correlated with the thicker clouds measured by HIRS (also see Jin, Rossow, & Wylie 1996). On this basis, it is reasonable to renormalize the HIRS data to include the thin clouds that the HIRS instrument cannot measure directly. To produce HIRS cloud covers in Hawaii comparable to those for SAGE II and experienced by the KAO, the required renormalization is approximately

$$C_{\rm HIRS}(x, y) = 0.2[10 f_{\rm HIRS}(x, y)], \quad (6)$$

where $f_{\rm cover}$ has again been assumed to be 0.2 (see eq. [5]). Paralleling SAGE II, the quantity $10 f_{\rm HIRS}$ then serves as an estimate of the fraction of flights that will encounter clouds and $C_{\rm HIRS}$ estimates the fraction of total flight time directly impacted by clouds (see § 5). It should be noted that this renormalization of the HIRS data assumes that the quantitative relationship of subvisible to visible clouds is the same everywhere. Although the correspondence of cloud patterns suggests that this is reasonable, the study of high-altitude subvisible cirrus is an area of active research, and the mechanisms of subvisible cirrus formation are not well understood.

3. THE WATER VAPOR OVERBURDEN

3.1. The Effects of Water Vapor on Airborne Astronomy

Water vapor is the principal molecular absorber throughout much of the infrared. Its strong vertical stratification at altitudes below the tropopause is one of the primary motivations for conducting airborne observations from the stratosphere, where the water vapor overburden is relatively small and roughly constant. Like high-altitude clouds, water vapor attenuates the light from infrared astronomical sources and increases sky noise by increasing the thermal background fluctuations seen by the detectors. As discussed by Erickson (1998), these effects are strongly dependent on the resolution of the instrument, the wavelengths under investigation, and the dominant noise source (e.g., pointing, photon noise, or modulations of the raw power). Considering a reasonable mixture of photometry and spectroscopy under a variety of observing conditions, Erickson estimates that an increase in the zenith water vapor overburden by 1 precipitable μm will require ~10% more observing time by SOFIA to obtain the same signal-to-noise ratio on the same objects. Erickson (1998) further points out that the time penalty is considerably greater in some cases (e.g., observations of the astrophysically important O I line at 63 μm or the extremely water-sensitive N II line at 122 μm).

The water vapor overburden at SOFIA flight altitudes has been measured by many KAO experiments over the past two decades (see, e.g., Nolt et al. 1979; Kuhn 1982), but the data have not been systematically archived and cover only a few selected geographic regions. Good temporal and spatial coverage of the globe must come from satellite observations. Typ-

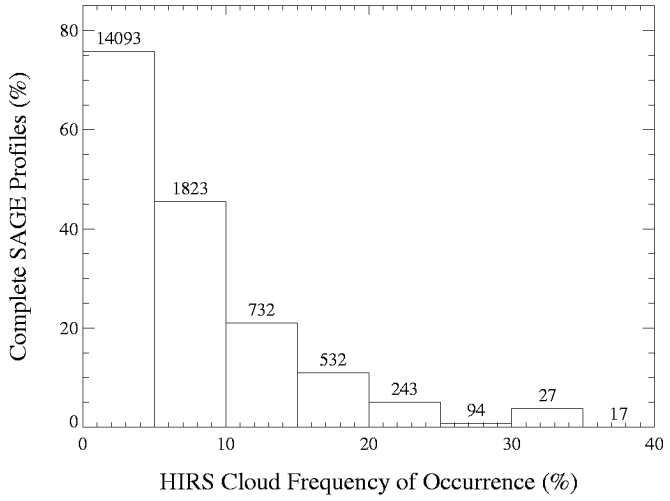

FIG. 1.—Percentage of profiles that SAGE II measured down to 179 mb vs. the HIRS frequency of cloud occurrence. This correlation is independent of season; the average of the four seasons is shown for all profiles between 0° and 60° N. Each bin is labeled with the total number of SAGE II profiles included.

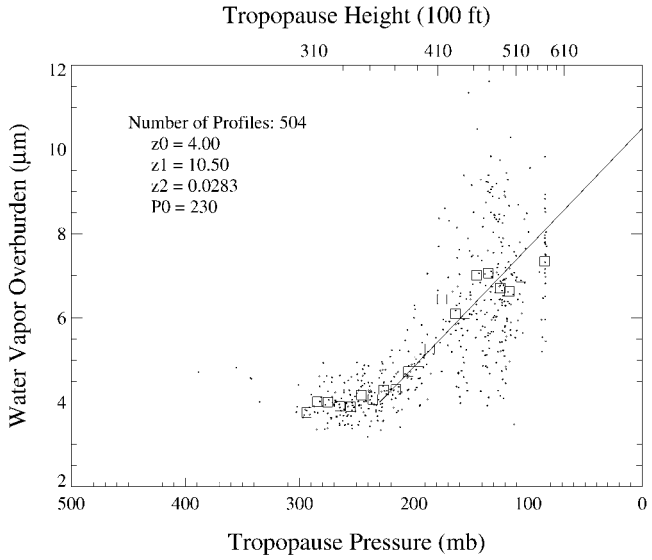

FIG. 2.—SAGE II zenith water vapor overburdens above 179 mb (FL410) as a function of tropopause pressure (or height) for the North American Region in summer. The dots represent integrations of individual SAGE II profiles, the boxes represent 10 mb averages, and the solid line is a fit. There are more data points on the flat portion of the curve at higher tropopause pressures in the other seasons.

ical zenith water vapor overburdens at FL410 are 5–20 precipitable μm or less than 1% of the overburden from dry mountain sites. The best available estimates are provided in the following two subsections.

3.2. The SAGE II/Tropopause-Height Water Vapor Overburden

The first estimate of the water vapor overburden comes from the SAGE II mixing ratio profiles (Rind et al. 1993). The individual profiles were retrieved from the NASA-Langley Distributed Active Archive Center (userserv@eosdis.larc.nasa.gov). For the period between 1986 January and 1991 May, when Mount Pinatubo erupted, there were a total of 4554 profiles that lie in the North American Region and extend down to at least 179 mb (FL410). Each of these profiles was vertically integrated to provide a zenith water vapor overburden, z', above 179 mb using

$$z' = -\frac{1}{g}\frac{M_{H_2O}}{M_{air}}\int_{179}^{10} q(P)dP, \qquad (7)$$

where M_{H_2O} is the molecular weight of water, M_{air} is the molecular weight of dry air, g is the gravitational acceleration, and $q(P)$ is the SAGE II mixing ratio at each pressure level, P, from 179 mb to the upper cutoff of the experiment at 10 mb.

In principle, these integrated profiles could be sorted by season and contoured to produce maps of zenith water vapor overburden as a function of position and altitude. However, this approach fails because of the sparseness of the data set—most seasonal/geographical bins have only a few data points, and some have none. The absence of sufficient data is particularly severe in cloudy regions because SAGE II only measures the water vapor mixing ratio in the absence of clouds. This "dry bias" is well known (Rind et al. 1993; Read et al. 1995) and occurs because water vapor and cloud abundance are highly correlated (§ 4), so cloudy regions have proportionately fewer successful SAGE II water vapor mixing ratio measurements and the successful ones necessarily occur on the driest days. This is illustrated in Figure 1, which plots the complete SAGE II profiles against the HIRS frequency of cloud occurrence (§ 2.3) at the same spatial/temporal locations. Since the SAGE II profiles occur primarily in the most cloud-free regions and always on cloud-free days, they represent a "clear-sky climatology." An analogous treatment of the UARS/HALOE (Russell et al. 1993) water vapor mixing ratio data provided by L. E. Deaver (private communication) finds similar dry biases.

Since sparseness precludes direct contouring of SAGE II data, a more statistical approach is used to produce a meaningful climatology. Each complete profile is correlated with the tropopause height at the time and place of the observation. The World Meteorological Organization (WMO) definition of the tropopause (Craig 1965, p. 23) is used, and its height is obtained from the National Weather Service's Global Data Assimilation System (GDAS) (http://spsosun.gsfc.nasa.gov/nmc_rev4.html#GDAS) as derived by the National Climate Prediction Center (R. M. Nagatani, private communication).

Figure 2 shows the resulting SAGE II water vapor overburdens, z', as a function of tropopause heights for the summer

season. This figure illustrates the fact that when the tropopause pressure is greater than 179 mb (tropopause below FL410), the water vapor mixing ratio is nearly constant at its stratospheric value (approximately 4 ppmv), and the zenith water vapor overburden is about 4 precipitable μm. On the other hand, when the tropopause pressure is less than 179 mb (tropopause above FL410), the zenith water vapor overburden is larger and much more variable from day to day. The magnitude of the effect is seasonal and is largest in the summer. Qualitatively similar results are obtained from 50 NASA ER-2 aircraft soundings using Lyα hygrometers (Kelly et al. 1993) and 30 balloonsondes using a frost point hygrometer (S. Oltmans, private communication).

To obtain estimates of the average zenith water vapor overburden as a function of geographic location, the overburdens in Figure 2 were fitted to provide an analytic expression for the average overburden as a function of the GDAS tropopause pressure, P_T. The functional dependence for the fit was assumed to be

$$z' = \max \{z_0, z_1 - z_2 P_T\}. \quad (8)$$

This curve has a constant value, z_0, above pressure P_0 [$= (z_1 - z_0)/z_2$] and has intercept z_1 and slope z_2 below P_0. This analysis was carried out for each season and flight altitude. The resulting values for the fit constants z_0, z_1, and z_2 are given in Table 1, along with P_0, the location of the "knee." This procedure is insensitive to the geographic region considered; the SAGE II data give fit constants virtually identical to those in Table 1 for 0°–60° north latitude and 40°–110° west, 110°–180° west, or all longitudes.

Figure 6 shows the geographic distributions of average tropopause height for each season, as derived from the daily GDAS data for 1986–1995. These distributions can be converted into maps of zenith water vapor overburden using equation (8) and the appropriate values of the constants z_0, z_1, and z_2 in Table 1 (tropopause height is shown in Fig. 6 to facilitate the discussion in § 4). This retrieval procedure is believed to provide an accurate assessment of the average water vapor overburden on cloud-free days as a function of season and location. It ignores the day-to-day variations in the water vapor overburden that are evident in Figure 2 and the even larger values anticipated on cloudy days (see § 5.2).

TABLE 1
SAGE II Overburden/Tropopause Height Fit Constants

Season	FL	z_0	z_1	z_2	P_0
Winter (DJF)	410	4.15	5.20	0.0050	210
	430	3.80	0.00	0.0000	…
	450	3.40	0.00	0.0000	…
Spring (MAM)	410	4.10	7.20	0.0145	210
	430	3.80	4.80	0.0053	190
	450	3.50	0.00	0.0000	…
Summer (JJA)	410	4.00	10.50	0.0283	230
	430	3.70	8.00	0.0195	220
	450	3.40	6.00	0.0137	190
Autumn (SON)	410	4.35	7.80	0.0138	250
	430	4.00	6.00	0.0083	240
	450	3.70	0.00	0.0000	…

3.3. The MLS-derived Water Vapor Overburden

A second estimate of the zenith overburden, which includes contributions from cloudy days, is obtained from the Microwave Limb Sounder (MLS; Barath et al. 1993) on board the *Upper Atmospheric Research Satellite* (*UARS*; Reber et al. 1993). This instrument vertically scans the Earth's limb from the surface up to 90 km using three microwave radiometers. The 205 GHz channel, originally designed for stratospheric retrievals of ClO (Waters et al. 1993), has also been used to measure the water vapor mixing ratio in the troposphere (Read et al. 1995). Because MLS performs a limb scan every 4.°1 of orbital arc on each of its 15 orbits per day, its sampling frequency and spatial resolution are considerably higher than for the water vapor retrievals from SAGE II (Rind et al. 1993). Moreover, because MLS operates in the microwave region, it is only minimally affected by clouds and, consequently, has virtually no dry bias of the type experienced by SAGE II (§ 3.2).

A comparison of the global water vapor climatology produced by Read et al. (1995) with the HIRS frequency of cloud occurrence (Fig. 5) shows the strong correlation between wet regions and cloudy regions expected on the basis of simple meteorological arguments (§ 4). Even the subtle differences between water and cloud cover (such as the greater width of the tropical wet regions with respect to the cloudy regions) are expected because the ice particles in the convective outflow regions evaporate, moistening the surrounding air. Still, this data set is comparatively new and unvalidated, and the originator (W. G. Read, private communication) acknowledges a "wet bias" in the driest regions, perhaps by a factor of 2. This is supported by comparisons with SAGE II in dry, cloud-free regions where SAGE II is expected to produce reliable averages.

Read et al. (1995) provide only the mean water vapor mixing ratio for the 100 mb layer centered at 215 mb or approximately the height range from 10 to 13 km. Since the mixing ratio increases rapidly with decreasing height, this band is dominated by its lower levels. To infer water vapor overburdens at SOFIA flight altitudes from MLS, the mixing ratio as a function of altitude is expressed in analytic form, normalized to the MLS mixing ratio at 215 mb, and vertically integrated. The SAGE II profiles are used to determine the analytic form for the mixing ratio. Above we argued for a dry bias in the SAGE II data on a *statistical* basis, as many of the wettest profiles go unmeasured because they have associated cloudiness along

the line of sight (see Fig. 1). However, the individual, measured SAGE II profiles have been validated (Larsen et al. 1993) and can be used in this analysis. Figure 3 shows the 358 SAGE II profiles for the North American Region with mixing ratios greater than 20 ppmv at 179 mb. The data are plotted on a log-linear scale to demonstrate that the sharp, upper tropospheric decrease in mixing ratio is well characterized by a unique scale height, h_0. These data were multiplied by $\exp[(h - 12)/h_0]$, averaged, and fitted to obtain the best-fit scale height, $h_0 = 1.3 \pm 0.1$ km. Hence, the mixing ratio in the upper atmosphere can be parameterized as

$$q(h) = \begin{cases} q(0)e^{-h/h_0} & \text{for } h < h', \\ 4 & \text{for } h \geq h', \end{cases} \tag{9}$$

where $h' = -h_0 \ln[4/q(0)]$ is the "knee" of the distribution.

In the simplest recovery scheme, the constant $q(0)$ can be determined by averaging $q(h)$ over the MLS band (10–13 km) and setting the result equal to the MLS mixing ratio. However, to account for the wet bias of MLS in dry regions, a more sophisticated correction scheme is employed that was suggested by W. G. Read (private communication). It relies on the fact that (1) the MLS retrieval method is most accurate at the levels where the water vapor mixing ratio is about 150 ppmv (Read et al. 1995) and (2) the vertical scale height of the MLS water vapor measurements is too large (W. G. Read, private communication). Thus, the scheme uses a characteristic scale height, $h_{\rm MLS}$, to determine a level between h_c and $h_c + 3$ km (field of view is 3 km, independent of height; Read et al. 1995) for every MLS mixing ratio, $q_{\rm MLS}$, where the height-averaged mixing ratio is 150 ppmv. In regions where the 215 mb mixing ratio is less (more) than 150 ppmv, h_c is less (more) than 10 km. The water vapor overburden is then calculated using an idealized profile (eq. [9]), a realistic scale height from SAGE II (h_0), and a value of $q(0)$ obtained from a height-averaged MLS value of 150 ppmv between h_c and $h_c + 3$. The detailed steps in this scheme are as follows:

Step 1.— The MLS mixing ratio in the upper atmosphere is parameterized as

$$q_{\rm MLS} = q_{\rm MLS}(0)e^{-h/h_{\rm MLS}}, \tag{10}$$

and the MLS scale height, $h_{\rm MLS}$, is determined from MLS mixing ratios at different pressure levels to be about 3.5 km (Read et al. 1995; Newell et al. 1996).

Step 2.—The defining equation for an MLS mixing ratio,

$$q_{\rm MLS} = \int_{10}^{13} q_{\rm MLS}(0)e^{-h/h_{\rm MLS}}dh \Big/ \int_{10}^{13} dh, \tag{11}$$

is inverted to solve for $q_{\rm MLS}(0)$ in terms of $q_{\rm MLS}$.

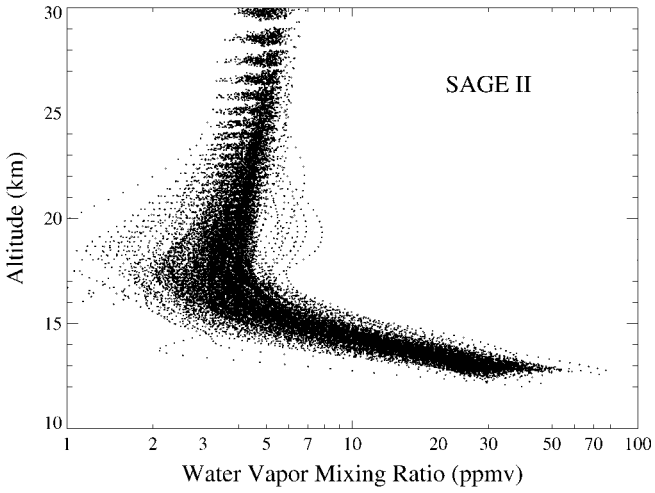

FIG. 3.—The 358 SAGE II water vapor mixing ratio profiles in the North American Region with $q(179\ \text{mb}) > 20$ ppmv.

Step 3.—Given $q_{\rm MLS}(0)$ and $h_{\rm MLS}$, the equation

$$\frac{1}{3}\int_{h_c}^{h_c+3} q_{\rm MLS}(0)e^{-h/h_{\rm MLS}} = 150\ \text{ppmv} \tag{12}$$

is solved for the height, h_c, which is the lower bound for the most accurate MLS band. The recovered values of h_c range from 7 km for $q_{\rm MLS} = 65$ ppmv to 12 km for $q_{\rm MLS} = 270$ ppmv. These are similar to the estimates given in Read et al. (1995) for the level of greatest sensitivity (and accuracy) for MLS as a function of $q_{\rm MLS}$.

Step 4.—The water vapor mixing ratio is parameterized by equation (9). The SAGE II scale height, $h_0 = 1.3$ km, is assumed and the constant $q(0)$ is determined by pinning the water vapor distribution at the best MLS level and solving

$$\frac{1}{3}\int_{h_c}^{h_c+3} q(0)e^{-h/h_0} = 150\ \text{ppmv}. \tag{13}$$

Step 5.—Zenith water vapor overburdens above flight level $h_{\rm FL}$ are then obtained from

$$z''(x, y) = \frac{M_{\rm H_2O}}{M_{\rm air}} \int_{h_{\rm FL}}^{\infty} \rho(h)q(h)dh, \tag{14}$$

where $q(h)$ is defined by equation (9), $q(0)$ is defined by equation (13), and

$$\rho(h) = 0.1786\ e^{-(h-12.5)/h_1} \tag{15}$$

is a good approximation to the upper tropospheric density de-

pendence for a scale height of $h_1 = 6.34$ km (US Standard Atmosphere 1962).

For $q_{MLS} = 50$, 100, 150, and 200 ppmv, the inferred overburdens at FL410 are 4.5, 6.4, 13.0, and 25.4 precipitable μm, respectively. The overburdens corresponding to $q_{MLS} = 50$ and 100 ppmv are only slightly higher than the SAGE II and UARS/HALOE (Russell et al. 1993; L. E. Deaver, private communication) values in dry regions (e.g., at FL410 over Moffett Field, CA, in DJF, MAM, JJA, and SON, respectively, our MLS retrieval scheme gives overburdens of 4.8, 5.1, 5.8, and 6.2 precipitable μm, SAGE II gives 4.2, 4.2, 6.1, and 5.4 precipitable μm, and HALOE gives 4.0, 4.1, 6.3, and 5.4 precipitable μm). The water vapor overburden for $q_{MLS} = 150$ ppmv is unchanged from the value derived when h_c is fixed at 10 km, since this is where MLS is already believed to be correct and needs no wet-bias correction. The overburden corresponding to $q_{MLS} = 200$ ppmv is sensitive to variations in h_{MLS}, increasing from 23 to 28 precipitable μm when h_{MLS} is increased from 3 to 4 km. However, these large overburdens are both unacceptable for SOFIA observations (Remmers 1996), so this uncertainty is relatively unimportant.

Figure 7 displays the zenith water vapor overburdens inferred from MLS, $z''(x, y)$, as a function of season for the North American Region. Values of $h_0 > 1.3$ km make $q(0)$ drop off more slowly with height and lead to somewhat larger values of z'', whereas smaller values of h_0 lead to smaller values of z''. This extrapolation procedure assumes, of course, that the mixing ratio scale height does not change with geographic location or season. At least for the dry profiles that SAGE II measures, there is no obvious bias of this type.

These water vapor overburdens are consistent with those observed on the KAO: Nolt et al. (1979) report values of 3.9–11.4 μm with a mean of 6.5 μm on 12 flights at FL410 out of Moffett Field in the fall of 1974; Nolt & Stearns (1980) found a mean value of 8.5 μm on 11 summer flights out of Hawaii; Erickson et al. (1979) report overburdens of 5–30 μm on five flights between 1976 and 1978; and Kuhn (1982) shows mean overburdens versus latitude and finds values from 7 to 15 μm at FL410 for the spring and summer seasons of 1976–1980. The Erickson group routinely measured KAO water vapor overburdens with their cooled grating spectrometer between 1984 and 1995. The lowest overburdens they observed on a flight out of Moffett Field were 3 μm at FL430 and 2 μm at FL450 in 1986 February (Lord et al. 1996); more typical values at FL410 ranged from 5 to 15 μm. A. W. Meyer (unpublished) compared the KAO radiometer with spectroscopic determinations of overburden and found that most values fell between 3 and 10 μm with extremes of 2 and 23 μm. There is no general archive of KAO overburdens versus location, season, and flight altitude.

4. DISCUSSION OF THE METEOROLOGICAL DATA

The SAGE II cloud data (Fig. 4), the HIRS cloud data (Fig. 5), and the MLS-derived water vapor overburdens (Fig. 7) display remarkable spatial and seasonal correlation. This is clear evidence of the validity and usefulness of these satellite data sets. This validity is further strengthened by consideration of the physical mechanisms and atmospheric circulations that produce high-altitude clouds and water vapor. As shown below, these data sets are consistent not only with each other but also with other independent meteorological observations of clouds and water vapor and known characteristics of the global atmospheric circulation.

4.1. The Meteorological Analyses

Much of our understanding of these phenomena comes from the extensive global data set that has been gathered over a significant depth of the atmosphere on a systematic basis during the past 50 yr. The cornerstone of this data set is the global system of sounding balloons, which simultaneously measure pressure, winds, temperature, and humidity to altitudes of 30 km twice per day. Over most of the Earth's land surface, the horizontal resolution of these data is about 350 km. More recently, these observations have been supplemented by aircraft wind observations and satellite temperature observations. This heterogeneous set of data, taken at a variety of times and in a spatially inhomogeneous manner, is used to derive the values of meteorological quantities (pressure, winds, temperature, and humidity) on a uniform grid in space and time. These gridded data sets, called analyses, are used for climatological studies and as initial conditions for forecast models. These analyses incorporate not only the observations, but the fundamental physics that governs atmospheric motion. Incorporating the basic physics is necessary to deal with two fundamental limitations of these observations: (1) large gaps in the data set (such as over the oceans) and (2) aliasing of small-scale phenomena into the generally larger scales realizable by the grids in the analyses.

The tropopause heights given in Figure 6 result from such analyses. Similarly, Figure 8 shows wind speeds (isotachs) and directions at FL410 over the North American Region for each season, and Figure 9 shows the corresponding geopotential heights. The isotachs indicate the locations of strong winds (or jet streams), while the geopotential heights, being approximate streamlines in the midlatitudes, show the direction of these winds. The actual wind directions are also shown in Figure 9 to illustrate their strong correlation with geopotential height. Figure 10 combines the HIRS clouds, the geopotential heights, and the wind directions on a global scale for the summer season to facilitate the discussion below. The data sets in Figures 8–10 (excluding HIRS in Fig. 10) are derived from the Goddard Earth Observing System Data Assimilation System—Version 1 (GEOS-1; Schubert, Rood, & Pfaendtner 1993). They show 2 yr averages (1994–1995) of 4 times daily analyses. Although data for GEOS-1 are available for longer periods, only during these 2 yr are they available on the finer $2\overset{\circ}{.}5 \times 2^\circ$ grid. For the

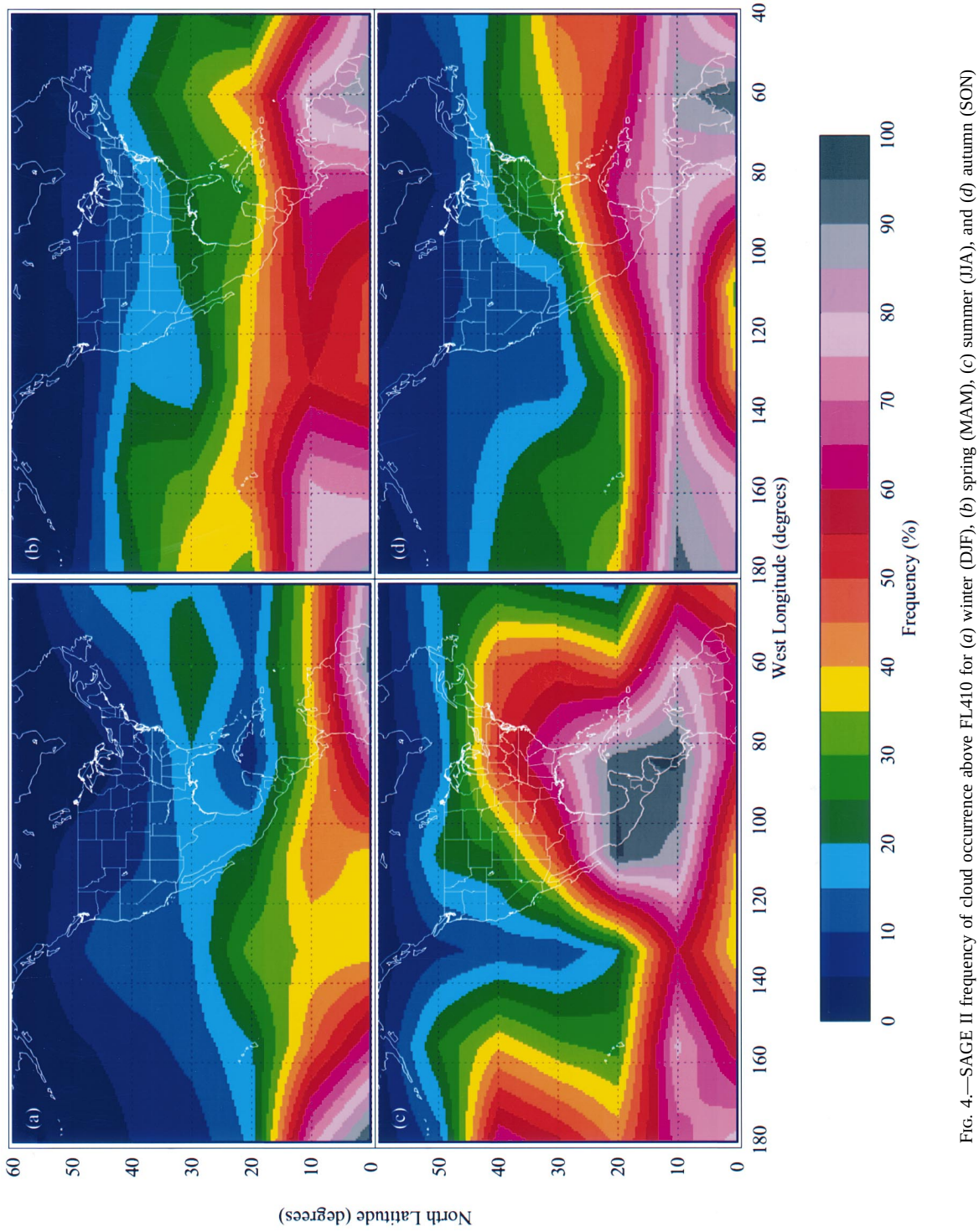

FIG. 4.—SAGE II frequency of cloud occurrence above FL410 for (*a*) winter (DJF), (*b*) spring (MAM), (*c*) summer (JJA), and (*d*) autumn (SON)

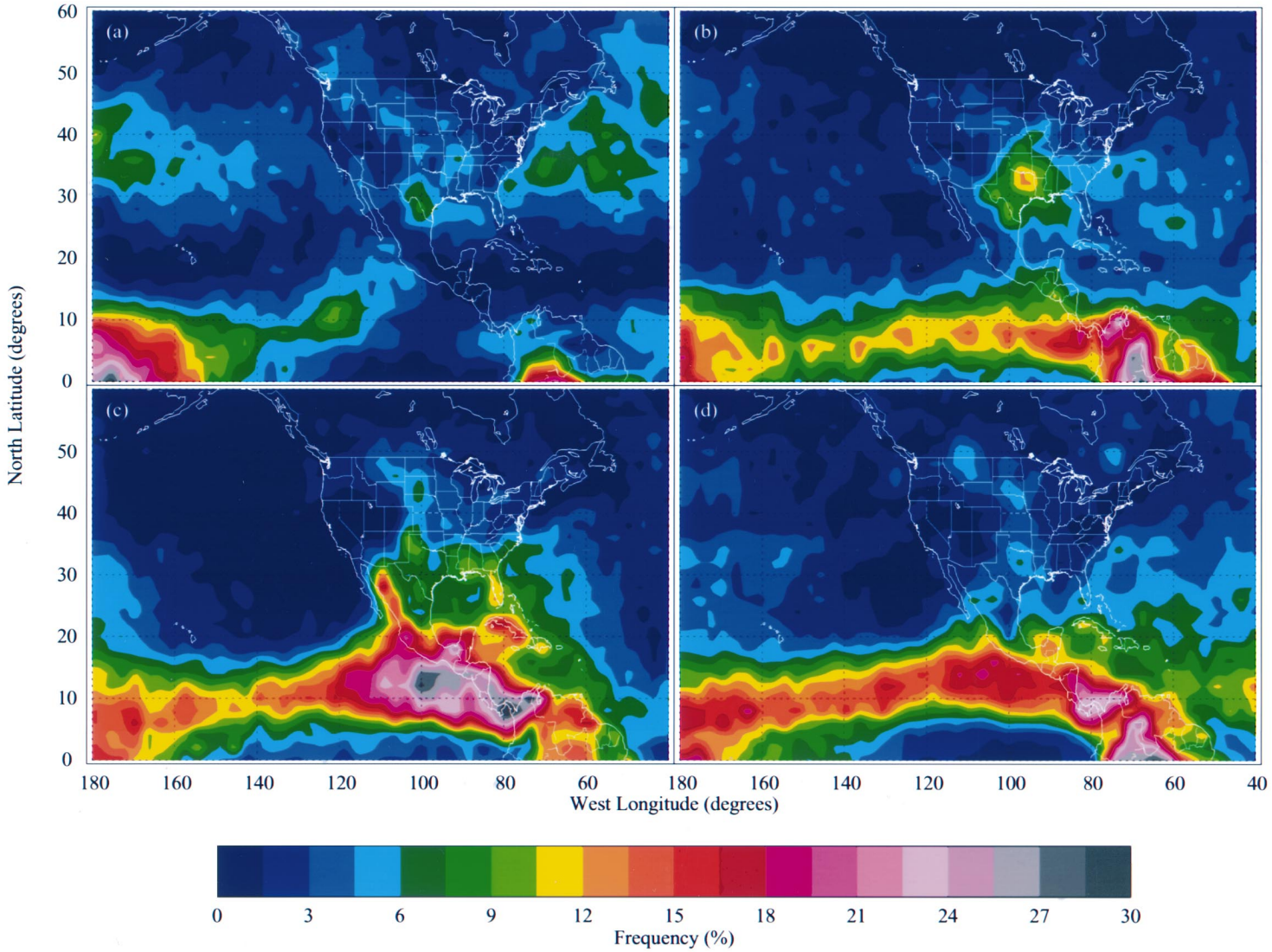

FIG. 5.—HIRS frequency of cloud occurrence above FL410 for (*a*) winter (DJF), (*b*) spring (MAM), (*c*) summer (JJA), and (*d*) autumn (SON)

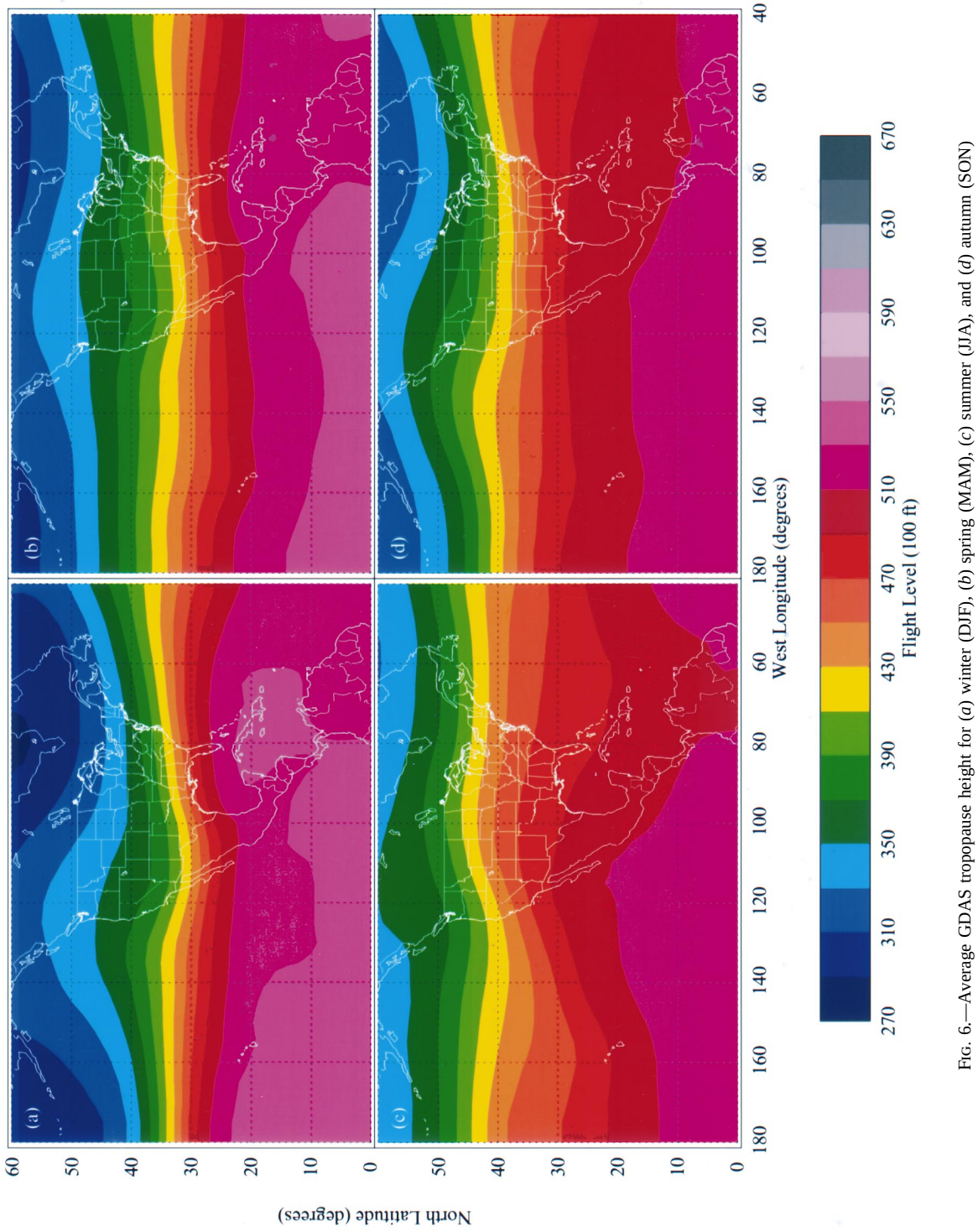

FIG. 6.—Average GDAS tropopause height for (*a*) winter (DJF), (*b*) spring (MAM), (*c*) summer (JJA), and (*d*) autumn (SON)

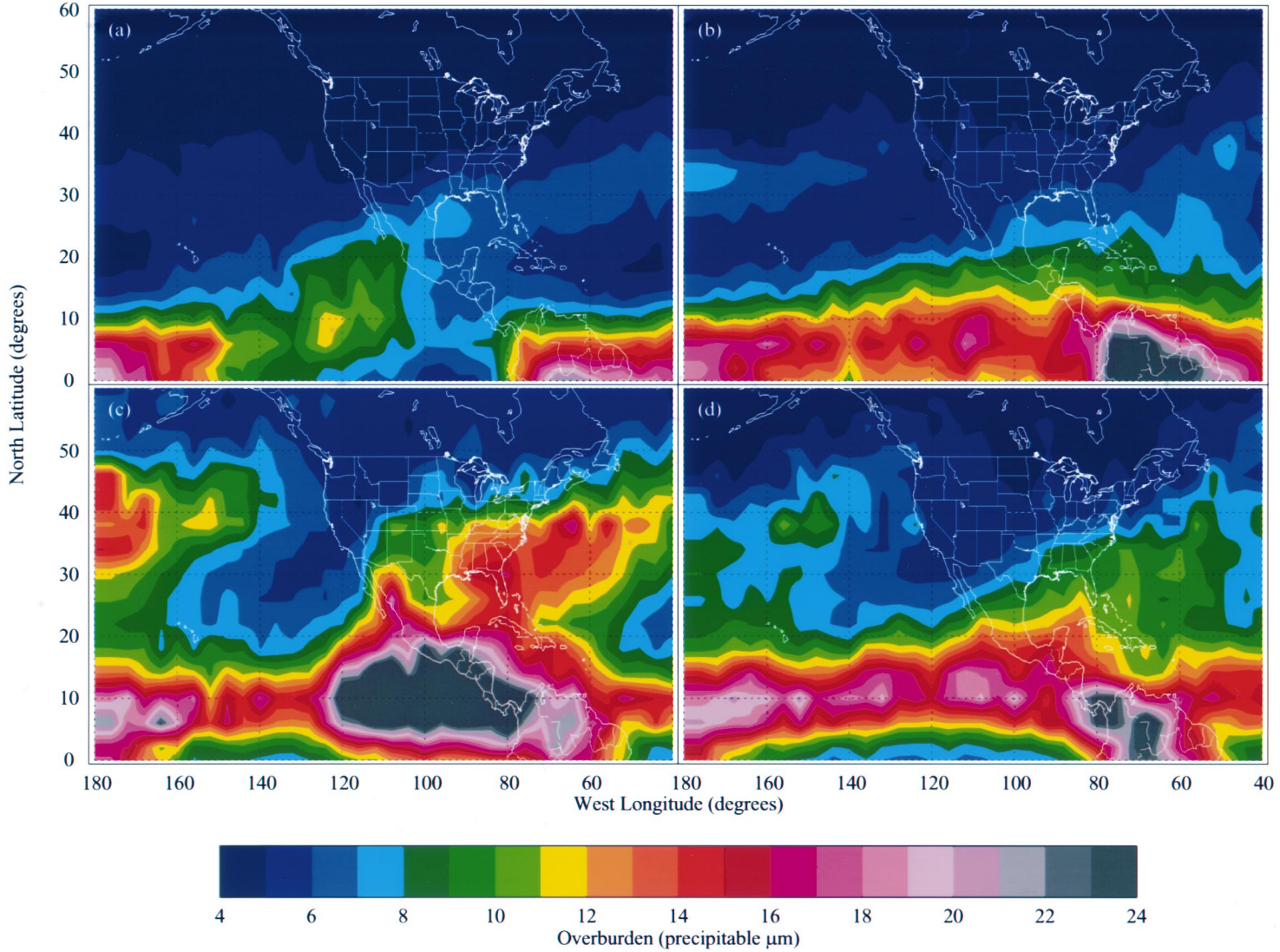

FIG. 7.—The MLS-determined zenith water vapor overburden for (*a*) winter (DJF), (*b*) spring (MAM), (*c*) summer (JJA), and (*d*) autumn (SON)

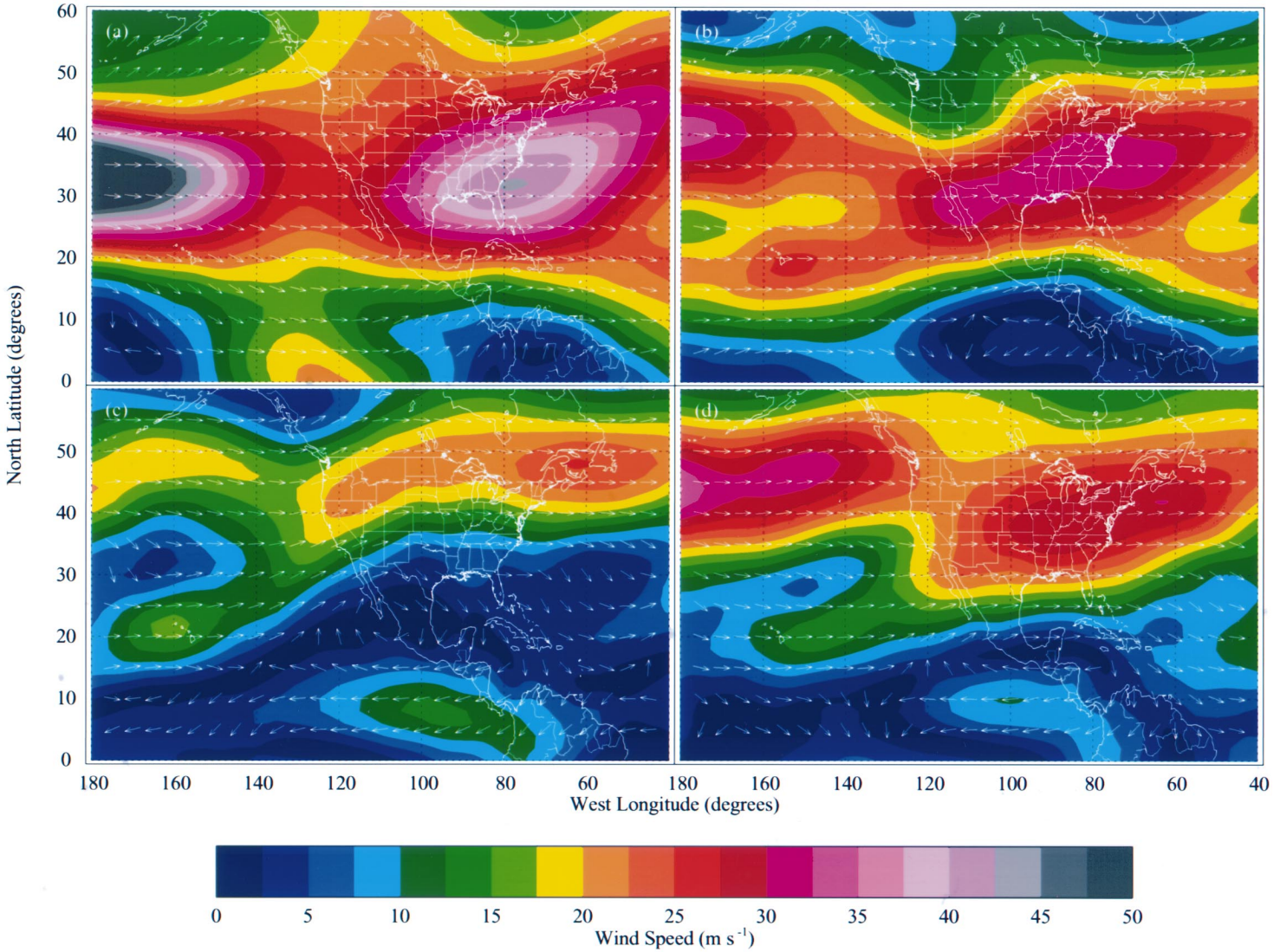

FIG. 8.—Wind speed (*contours*) and wind direction (*arrows*) at FL410 for (*a*) winter (DJF), (*b*) spring (MAM), (*c*) summer (JJA), and (*d*) autumn (SON)

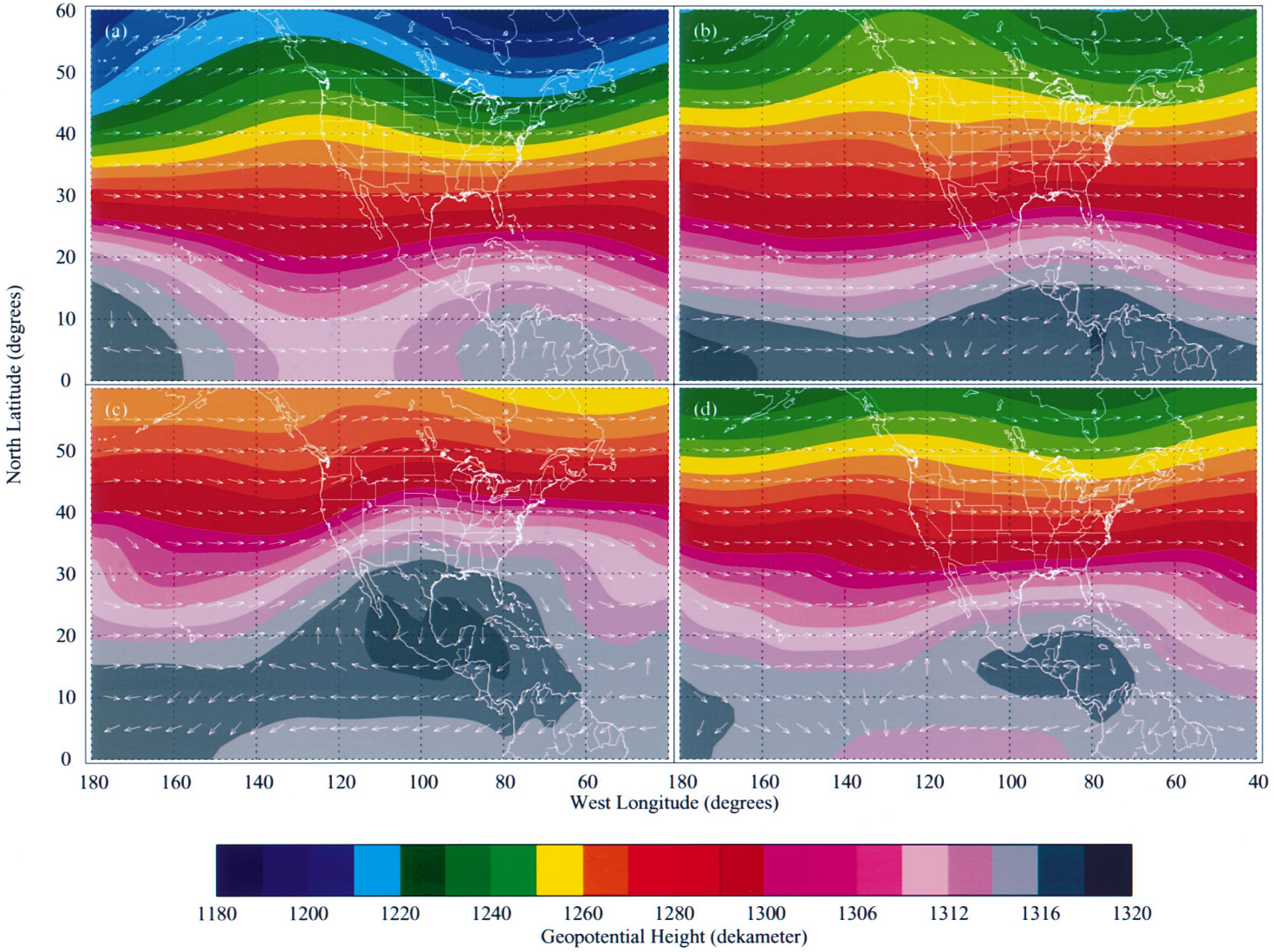

FIG. 9.—Geopotential height (*contours*) and the wind direction (*arrows*) at FL410 for (*a*) winter (DJF), (*b*) spring (MAM), (*c*) summer (JJA), and (*d*) autumn (SON)

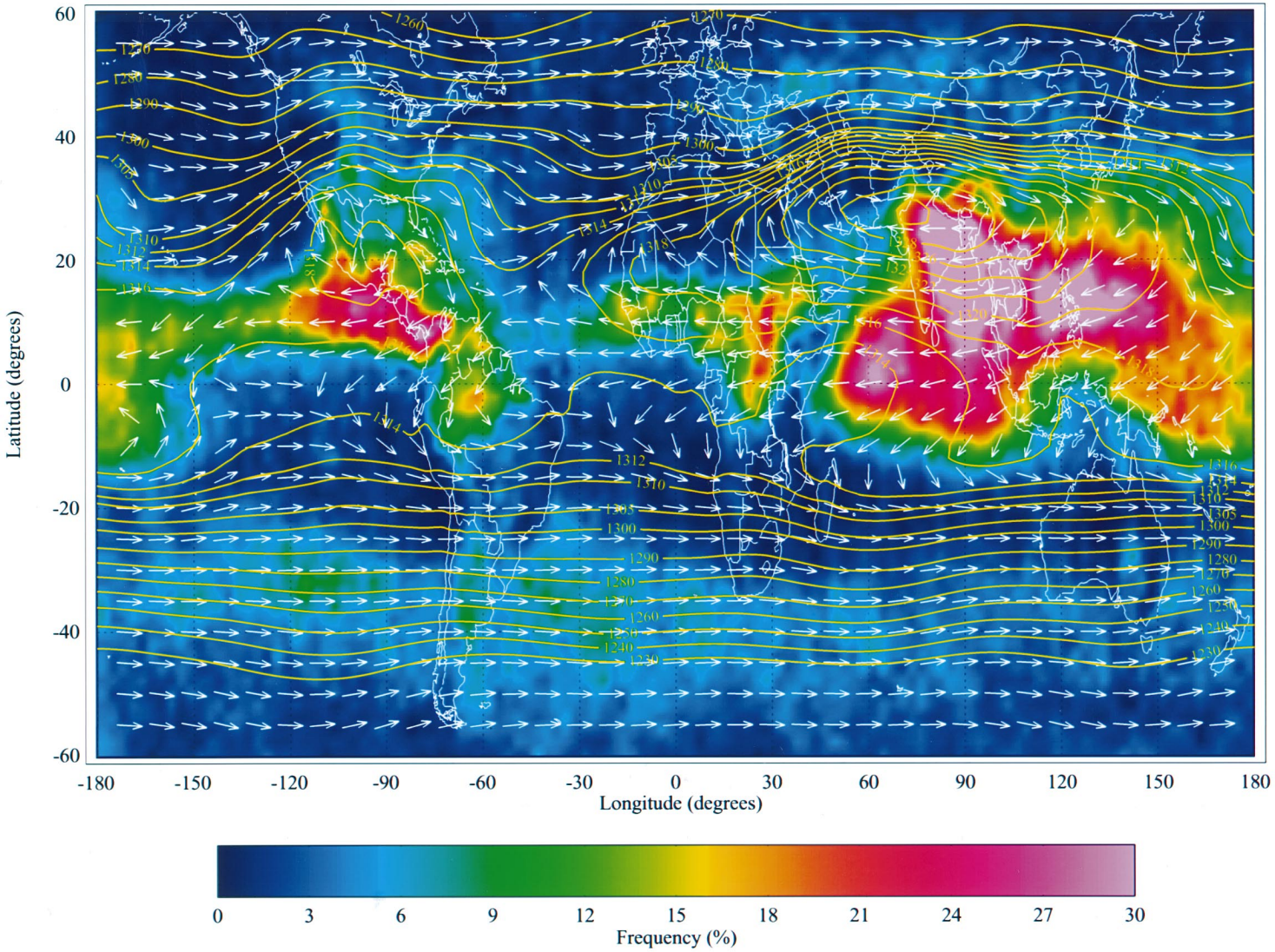

FIG. 10.—Geopotential height (contours labeled in dekameters) and the wind direction (*arrows*) at FL410 superimposed on the HIRS frequency of cloud occurrence above FL410 (*color table*) on a global scale for the summer season.

purposes of this paper, the features of interest are persistent enough that a 2 yr average is sufficient.

4.2. Physical and Meteorological Considerations

The cloud and water vapor distributions in the upper troposphere should be correlated, since one is merely the condensed state of the other. It is important to realize, however, that the upper troposphere is far removed from the ultimate reservoir of water, namely the oceans, and that moisture is constantly being removed from the atmosphere by precipitation processes. Thus, the mechanisms of upward moisture transport are the first consideration in understanding upper tropospheric clouds and water. The second consideration involves the sources of vertical motion in the atmosphere, since it is upward vertical motion that produces the adiabatic cooling that leads to condensation and the formation of clouds. The third and final consideration is the distribution of tropopause heights, as the tropopause serves as the upper limit of both cloud formation and significant relative humidity. The first two considerations are related, since upward water transport involves vertical motion. However, much upper tropospheric cloudiness is produced by upward motions that extend over fairly small depths. These shallow motions are not a factor in net upward (or downward) water vapor transport, although they do make significant contributions to the integrated upper tropospheric moisture budget through precipitation from clouds. Thus, vertical motion will be considered separately.

4.2.1. Mechanisms of Upward Moisture Transport

There are two basic mechanisms by which moisture is transported to the upper troposphere: deep moist convection in the tropics and midlatitudes, and pseudoadiabatic motions associated with large-scale, midlatitude cyclones. Deep convection carries ice particles upward until a stabilization level is reached and the vertical flow diverges, carrying much of the ice with it. The result is the familiar cumulus anvil shape of deep convective clouds (see, e.g., Johnson, Gallus, & Vescio 1990). These anvils can extend over many hundreds of kilometers at or just below the tropopause level (Prabhakara et al. 1993). Eventually, most of the ice falls out, some reaching the ground as precipitation and some evaporating in the intervening air. The smallest ice particles will essentially stay with the flow and evaporate as the air descends in the regions surrounding the convection, providing a moisture source for the highest parts of the troposphere. The deepest systems will reach the tropopause, even penetrating into the stratosphere (Danielsen 1982), although the bulk of the convective outflow for large tropical systems actually occurs over significant depths (10–16 km; Houze 1989). Midlatitude deep convection, although much less widespread than tropical convection, also transports moisture to the tropopause region (Johnson et al. 1990), particularly in the spring and summer seasons (see below). The vertical motions associated with large-scale (1000 km or more), midlatitude cyclones also act as a source of moisture for the upper troposphere. In these systems, moist air from midlevels in the tropics (5–7 km—deposited there by midlevel convection) is advected poleward ahead of the low centers (Palmén & Newton 1969, p. 310), rising as it follows the isentropic surfaces, which have a mean upward and poleward slope at altitudes up to the midlatitude tropopause (Danielsen, Gaines, & Hipskind 1983).

4.2.2. Vertical Motions in the Upper Atmosphere

The second consideration in the distribution of upper tropospheric clouds and moisture is vertical motion. Sources of vertical motion include the deep moist convection discussed above, but these systems occupy only a small area at any given time. In fact, in the tropics and subtropics, outside of the large-scale convective regions (e.g., the region near 12° north, 99° west in Fig. 5*c*), air tends to descend, owing both to the slopes of the isentropic surfaces and to radiative cooling (Doherty, Newell, & Danielsen 1984). Thus, the relative humidity is fairly low in the subtropical, and much of the tropical, upper troposphere outside of convective regions (Soden & Bretherton 1993). In the presence of dynamically induced lifting, however, the moisture deposited in the upper troposphere by convection will condense, resulting in sheets of high-altitude cirrus haze (Jensen et al. 1996). In the tropics, such lifting is probably due to large and synoptic scale tropical waves (see, e.g., Tsuda et al. 1994), whereas in midlatitudes, such lifting will be induced by cyclonic disturbances in the prevailing westerly jet stream.

The same large-scale, midlatitude cyclones that move moisture into the upper troposphere can also produce high-altitude cloudiness. This is partially a result of the precipitating weather fronts associated with these cyclones, but most of the high-altitude cloudiness in midlatitudes is not directly related to any surface disturbance (Mace et al. 1995). Instead, high cloudiness is produced largely by the circulations around the high-altitude jet streams (regions of very strong upper tropospheric winds) that are associated with the large-scale cyclones (Starr & Wylie 1990). Entrance and exit regions of these jet streams, together with the strong upward and downward motions on either side that are required to produce the flow accelerations and decelerations, are likely regions for extensive high cloudiness. An example of cirrus due to these vertical motions is documented by Mace et al. (1995). The importance of these sources of vertical motion to the climatological distribution of clouds as a whole is reflected in the fact that cirrus (or high) clouds are the predominant type over most of the continental US and Hawaii, with incidences of 50% or more (Warren et al. 1986). The exception is the California coast, where low stratus clouds are the dominant type (Warren et al. 1986).

Vertical motions on still smaller scales are also important to cirrus cloud production. These smaller scales, and their global distribution, determine the character of the noise that such clouds produce in airborne astronomical observations (see § 2.1). The high-level fronts associated with jet streams

often have scales of a few hundred kilometers, which are reflected in the cirrus cloud structure (Starr & Wylie 1990). Another candidate is small-scale (5–200 km) gravity waves excited by flow over irregular terrain. These can generate distinctive wave clouds over mountain peaks, as well as variations within existing cirrus clouds. Even smaller scales of vertical motion contribute to producing and modifying the structure of cirrus clouds. Recent field studies have shown distinct, observable structures down to 200 m (Gultepe & Starr 1995). These scales are due to turbulence arising from strong shears and the subsequent decay of that turbulence into two-dimensional vortices. The presence of turbulence implies that there is significant variance on even smaller scales, including those in the tens of meters range that will most strongly affect astronomical observations (§ 2.1). There is no reason to expect a correlation between cirrus clouds formed by regional scale uplift due to cyclonic storms and the development of the strong shears that lead to turbulence and very small scales. However, it is clear that turbulence is most likely to occur over mountainous terrain and least likely over oceans, with flat terrain having an intermediate level of turbulence occurrence (Lilly, Waco, & Adelfang 1974).

4.2.3. The Importance of the Tropopause

The final consideration in understanding the upper tropospheric water vapor and cloud distribution is the significance of the tropopause. The tropopause is a sharp boundary region (less than 1 km thick), where vertical temperature gradients change from negative to positive, or isothermal. The resulting increase in vertical stability places a lid on the rapid vertical transport of moisture in the Earth's atmosphere. In fact, the mixing ratio of water in the stratosphere is limited to 2–6 ppmv by freeze drying at the tropical tropopause (see Fig. 3). These low mixing ratios, combined with the fact that temperature increases with altitude above the tropopause, create conditions that make cloud formation almost impossible (except for extreme situations like the lower polar winter stratosphere and the summer mesopause at 90 km).

The importance of the tropopause as an upper boundary for cloud formation is supported by recent ground-based lidar studies at a variety of locations, including sites in Virginia and Kansas (Winker & Vaughan 1994; Uttal et al. 1995). All of the retrieved distributions of cloud tops show a peak in the upper troposphere within 1–2 km of the tropopause. Similar cloud distributions are apparent in very preliminary data from the Lidar In-space Technology Experiment (LITE) flown on the NASA Space Shuttle during 1994 September (D. M. Winker, private communication). The physical explanation for this peak is still a subject of active research, but one likely factor is the strong vertical circulation associated with the jet streams near the midlatitude tropopause that were mentioned above. In convective regions, the fact that the strongest systems reach, but do not significantly exceed, the tropopause is probably responsible for the enhanced upper tropospheric cloudiness.

4.3. Comparison of Various Cloud Climatologies

The observed circulation patterns presented in § 4.1 (Figs. 8–10) and the basic meteorological considerations discussed in § 4.2 are reflected in the upper tropospheric/lower stratospheric weather measured by SAGE II, HIRS, and MLS. To illustrate, the relationships of the measured cloud and water vapor distributions to the circulation are discussed for each season individually.

4.3.1. The Winter Season (DJF)

For the winter season, the HIRS incidence of clouds above FL410 is shown in Figure 5*a*. There are several regions of enhanced high cloudiness. The tropical regions (less than 10° north) stand out, owing to the presence of deep convection and the very high tropopause (~16 km). Since it is winter, this convection is generally south of the equator, both in the central Pacific and over South America. The general features, including the peak over South America, the minimum of convection in the eastern equatorial Pacific, and the east-northeastward extension from the equator at 145° west toward the Mexican coast are also apparent in the SAGE II cloud frequency (Fig. 4*a*) and are consistent with other cloud climatologies focusing on deep, high convection, such as the highly reflective cloud climatology of Garcia (1985). These features are also consistent with our knowledge of the general circulation, showing strong upward mean meridional motion south of the equator during the Northern Hemisphere winter season (Oort & Rasmusson 1970). The relative absence of convection in the equatorial eastern Pacific is consistent with the very cold sea surface temperatures observed off the west coast of South America, with a tongue of relatively cold water extending westward south of the equator (see Plate 1 in Bottomley et al. 1990). These cloud features are also reflected in the MLS water vapor overburdens shown in Figure 7*a*. The horizontal extent of the enhanced water vapor overburden is actually greater than that of the HIRS clouds. This is consistent with the work of Udelhofen & Hartmann (1995) using *GOES* 6.5 μm data (which probes somewhat lower altitudes than MLS). They found that convection moistens the upper troposphere within about 500 km of the areas of enhanced convection.

A second region of enhanced HIRS cloudiness (Fig. 5*a*) and MLS water vapor (Fig. 7*a*) lies in the midlatitudes, between 30° and 40° north in the Pacific and on a southwest-northeast track from Texas into the north Atlantic. These regions of cloudiness are produced by midlatitude cyclonic disturbances and the associated jet stream circulations discussed in § 4.2. This is well illustrated by the strong correspondence between the cloud distribution (Fig. 5*a*) and the jet streams in the eastern Pacific and southeastern US/Atlantic (Fig. 8*a*). These jet streams coincide roughly with those areas in which the equator-

to-pole temperature gradients are particularly intense, consistent with the dynamical relationship between these temperature gradients and the vertical wind shear (which results in strong winds in the upper troposphere by vertical integration). These temperature gradients are the energy source for the cyclonic disturbances that generate the cloud-producing vertical circulations. The region of cloudiness in the Pacific coincides roughly with the Pacific wind maximum, while the cloudiness in the Gulf of Mexico and the Atlantic coincides with the southeastern US/Atlantic wind maximum. The region of reduced cloudiness at midlatitudes from California to the Great Plains coincides with a region of weaker horizontal temperature gradients and weaker 180 mb winds. The maximum in cloudiness over south Texas coincides with the Atlantic Polar Front jet entrance region. This behavior is consistent with expectations, given the strong vertical circulations associated with jet entrance regions (Keyser & Shapiro 1986).

The MLS water vapor overburdens display a similar midlatitude maximum associated with the jet streams. However, the MLS maximum is weaker and is displaced southward relative to the HIRS cloudiness maximum. This is actually quite reasonable because (1) the HIRS cloudiness is a "digital" quantity (each observation is designated as either "cloudy" or "not cloudy"), while the MLS water vapor overburden has a continuous range of values; and (2) the altitude of the tropopause decreases rapidly with latitude in midlatitudes during the winter season. In fact, the mean tropopause is actually at or below FL410 in the midoceanic portions of the midlatitude cloudiness maximum (see Figs. 5*a* and 6*a*). Since the high clouds are concentrated near the tropopause (see above), fluctuations in tropopause height associated with cyclonic storms can yield significant cloud incidence above FL410 even when the mean tropopause is below that level. However, the average water vapor in those regions is more likely to be driven by the low stratospheric values that occur when the tropopause is below FL410. Thus, the water vapor maximum is displaced southward toward higher tropopause heights.

In fact, the low tropopause heights in winter are responsible for the generally low incidence of clouds and small water vapor overburdens above FL410 over the continental US, with the exception of the south central and southeastern US (where FL410 is at or below the mean tropopause—Fig. 6*a*). However, the data for this season demonstrate that tropopause height is by no means the only factor in determining the high-altitude cloud and water vapor distributions. For example, Hawaii, with a very high tropopause, has a fairly low incidence of clouds above FL410. This is due to the fact that Hawaii is in a region of downward vertical motion, being in the subtropical downward branch of the Hadley cell (Oort & Rasmusson 1970), which inhibits the formation of clouds. The cloudiness minimum associated with the downward branch of the Hadley cell is also present in the SAGE II data, as shown by the minimum over the Caribbean. In contrast, the south central and southeastern US, with a much lower tropopause, have a higher cloud incidence due to the presence of the strong vertical circulation discussed above.

4.3.2. The Spring Season (*MAM*)

During the spring season, the HIRS clouds (Fig. 5*b*) and the MLS-derived overburdens (Fig. 7*b*) show the following notable features: (1) The high clouds and water vapor produced by tropical convection have moved northward, forming a distinct line at 0°–10° north with a strong enhancement over South America. These features are consistent with other climatologies that focus on the deepest, highest clouds in the tropics (see, e.g., Garcia 1985). (2) The cloudiness associated with the storm tracks over the oceans has decreased markedly (although the water vapor overburden, particularly in the midlatitude Pacific, has increased somewhat, a feature probably due to the increase in mean tropopause height there; compare Figs. 6*a* and 6*b* with Figs. 7*a* and 7*b*). The decrease in midlatitude cloudiness arises from the weakening of the equator-to-pole temperature contrast associated with the Sun's northward movement as spring progresses. This weakening temperature gradient implies a weaker jet stream, which is clearly evident by comparing the isotachs in Figures 8*a* and 8*b*. Since this temperature contrast provides the energy source for the development of the midlatitude cyclones that produce the high midlatitude clouds, a decrease in midlatitude cloudiness is not surprising. (3) There is a region of enhanced high cloudiness over the south central US as a consequence of enhanced convective activity in this region in spring. This is a major feature that is apparent in the HIRS data for each of the individual spring months and at a broad range of altitudes.

This convective activity results from a set of conditions that is rarely found elsewhere on the globe: (1) the northwestward advection of warm moist air at the surface (heated by the increasing amount of sunlight) from the Gulf of Mexico into the south central US and (2) the northeastward advection of hot and dry air at midlevels over the warm moist air by the still fairly strong vertical shear associated with the midlatitude jet (Emanuel 1994; Palmén & Newton 1969). In fact, as a comparison of the isotachs in Figures 8*a*–8*d* shows, only in the winter season is the jet stream stronger than in the springtime. These conditions result in some of the most violent convection on the globe during late spring and early summer (Emanuel 1994). The resulting thunderstorms invariably reach the tropopause, producing extensive anvil outflows and depositing moisture at high levels that can contribute to cirrus cloud formation.

Curiously, except for a northward bulge in the tropical maximum at the longitude of the central US, this feature, so evident in the HIRS data, is almost absent from the MLS water vapor overburden (its absence in the SAGE II data can be ascribed to limited sampling in time and space relative to the area of the feature). This difference in the data sets is not fully understood. However, as indicated above, the spring thunderstorm

season in the south central US occurs as a result of large variations in winds and temperature on a subcontinental scale, a variability that is driven by instability in the midlatitude jet. It is quite reasonable to surmise that these instabilities involve substantial variability in upper tropospheric water as well. In this way the central US convection in the spring contrasts with tropical convection, which takes place in an environment in which the large-scale variability is fairly small. Spring thunderstorms in the south central US occur to the east of deep midlatitude troughs that produce the conditions favorable for the violent convection discussed in the previous paragraph. As these deep troughs propagate eastward, they bring dry (even stratospheric) air to the 200 mb region observed by MLS. Thus, the disagreement between MLS water vapor and HIRS clouds may well be due to the differing ways that time averaging affects a "digital" quantity such as clouds and a more "analog" quantity such as water vapor. Verification of this hypothesis requires an examination of the daily data that is beyond the scope of this work.

4.3.3. The Summer Season (JJA)

Figure 5*c* shows HIRS cloud frequencies for the summer season. During this season, tropopause heights (Fig. 6*c*) are the highest of the year, and, not surprisingly, this is reflected in the generally greater incidence of SAGE II and HIRS clouds and the increased MLS water vapor overburdens over much of the US. During this season, the high-cloud distribution is dominated by convective activity in the tropics and its extensions into the central part of the North American continent. Unlike the winter and spring seasons, there is little evidence of clouds at this level from the midlatitude jet stream (compare Figs. 5*c* and 8*c*). This is due to the weaker equator-to-pole temperature difference, which results in the weakest jet stream winds of the year. Since this is the energy source for midlatitude storms and jet stream disturbances, one expects a reduction in jet stream clouds. In the tropics (south of 20° north), the most important features are the line of high clouds in the central Pacific near 10° north (the intertropical convergence zone or ITCZ) and the prominent maxima over Central America and the Pacific south of Mexico. These features are clearly reproduced both in the MLS data (Fig. 7*c*), the SAGE II data (Fig. 4*c*), and the highly reflective cloud climatology of Garcia (1985).

In addition to the tropical features, there are strong enhancements in high cloudiness over western Mexico and the southwestern US, above and east of the Rocky Mountains in the US, and around the northern and eastern edges of the Gulf of Mexico. As shown by the overall lightning activity measured by the Optical Transient Detector (OTD) aboard a polar orbiting satellite (Christian, Blakeslee, & Goodman 1989; see the OTD Web Site, http://wwwghcc.msfc.nasa.gov/otd.html, for the actual monthly data), these regions are all well known for their extensive thunderstorm activity during spring and summer, which implies intense strong convection that reaches the tropopause (see, e.g., Johnson et al. 1990). The relatively narrow strip of high cloudiness in western Mexico that pokes northward into the southwestern US corresponds well with a region of high precipitation over the Sierra Madre Occidental (Douglas, Maddox, & Howard 1993). In fact, this well-known phenomenon is so strong and its effect on the regional circulation so pervasive that Douglas et al. refer to it as the "Mexican monsoon."

The HIRS cloud occurrence in Figure 5*c* also shows an extensive region of very minimal cloudiness in the eastern subtropical Pacific. This feature can be easily understood by examining the global high cloudiness pattern in conjunction with the global circulation at these levels. Figure 10 shows the global HIRS cloud frequency above FL410 and the GEOS-1 wind vectors and geopotential heights at FL410. The most prominent cloud feature is the strong zonal asymmetry on a global scale. There is one large region of extensive high cloudiness over east Asia and the western Pacific (70°–150° east) and a second, smaller region of high cloudiness centered over Central America (70°–120° west). These two cloudy regions are separated by areas of minimal high clouds, one in the eastern Pacific and western third of the US and the other over the eastern Atlantic and the Sahara and Arabian deserts.

This longitudinal variation in cloudiness correlates well with the longitudinal variations in the atmospheric circulation, and these circulation patterns provide an explanation for the suppressed cloudiness in the eastern subtropical Pacific and the Atlantic oceans. As documented by Krishnamurti (1971), White (1982), and others, the Northern Hemisphere summer circulation in the upper troposphere south of 45° north is dominated by the so-called Tibetan anticyclone. This anticyclone is essentially a large high-pressure region over Asia, as shown by the geopotential heights and the clockwise circulation around that high-pressure region in Figure 10. This anticyclone is a result of (1) the release of latent heat by the moist convection in south Asia, east Asia, and the western Pacific and (2) the sensible heating of the atmosphere by the elevated heat source of the Tibetan plateau. The atmosphere responds to this heating with upward motion, which is terminated at the tropopause because of the high static stability and consequent resistance to vertical motion. The resulting divergent flow at the top of the troposphere, combined with the Earth's rotation, produces the clockwise flow pattern (anticyclonic or negative relative vorticity) that is apparent in Figure 10. The maximum upward motion, cloudiness, and divergence is actually somewhat southeast of the center of the anticyclone. This is explained by the steady state vorticity balance, where the production of negative vorticity by divergence is balanced by the advection of positive planetary vorticity due to the southward winds on the eastern side of the anticyclone (Holton & Colton 1972; Webster 1972; White 1982). The same situation, with weaker amplitude, prevails over the North American land mass. Here the convection over the mountains of western Mexico, over the Rocky Mountains, and around the Gulf of Mexico produces net upward

motion in the region between 70° and 120° west. The divergence at the top of the troposphere generates an anticyclone. Again, owing to vorticity dynamics, the vertical velocities and cloudiness are displaced somewhat southeast of the anticyclone's center.

At the top of the troposphere, between these two anticyclonic centers of divergence and their accompanying upward motion, there are two basic regions of convergence and their accompanying downward motion. These form the well-known mid-oceanic troughs: the mid-Pacific trough and the weaker mid-Atlantic trough (Krishnamurti 1971). The convergence in these regions, combined with the Earth's rotation, produces counterclockwise rotation and positive vorticity. This positive vorticity exhibits itself as a southward excursion in the mean westerly flow in the upper troposphere, as shown by the wind arrows and geopotential heights in Figure 10. These troughs are roughly at the longitudes of Hawaii and about 30° west. As with the anticyclones, the vorticity dynamics dictate that the downward motion is slightly to the east of the troughs. In the case of the Pacific trough, this means that the strongest downward motion is east of Hawaii, which is consistent with the distribution of high clouds in the Pacific.

The summer mean upper tropospheric, vertical circulation patterns explain the planetary scale features in the high-cloud distribution. However, the high-cloud (Figs. 5*c* and 10) and moisture (Fig. 7*c*) distributions also display some sharper gradients which result from the details of the moisture sources for the upper troposphere and the advection of moisture from those sources by the upper level circulation. For example, off the west coast of Mexico, there is a very sharp gradient in high clouds. Here the cold sea surface temperatures strongly limit any possibility of moist convection north of 25° north, thus limiting the supply of moisture to upper levels (see Plate 7 in Bottomley et al. 1990). The upper level flow north of 25°–30° north is from the mid-Pacific trough region, where air has been heated and dried by downward motion. Just to the east, convection is enhanced by the elevated heat source represented by the Sierra Madre Occidental. The result is a strong gradient in the incidence of high clouds as one goes inland from the Pacific into the North American continent. In the Atlantic and the Gulf of Mexico, the low-level air is moister, owing to the generally higher sea-surface temperatures (Newell et al. 1973). This, along with the eastward and northward low-level flow associated with the mid-Atlantic surface high-pressure system, helps drive the convection over the south central and southeastern US. The upper level flow, in turn, advects the outflow of these convective systems eastward, away from the Pacific coast.

Although the SAGE II horizontal resolution is relatively poor, the same general features seen in the HIRS data (Figs. 5c and 10) are reproduced in the SAGE II data (Fig. 4*c*) and the frequencies of cloud occurrence are comparable after accounting for differences in optical depth (§ 2). This again indicates that the same basic processes and circulation patterns are driving the distribution of subvisible (SAGE II) and visible (HIRS) clouds. Notice in particular that almost any location east of the Colorado river and south of the Mason-Dixon line in the continental US has a higher incidence of clouds above FL410 than does Hawaii. Moreover, this is entirely consistent with the basic meteorology—the high incidence of moist convection east of the Rockies, the depth of that convection, and the fact that the tropopause is above FL410 everywhere in the US except for its most northern tier (Fig. 6*c*).

4.3.4. The Autumn Season (*SON*)

Figure 5*d* shows the HIRS distribution of high clouds during autumn. Like spring, this season can be viewed as a transition between winter and summer. Although the tropical convection has not moved south substantially, the reduction in solar heating north of the equator leads to less intense convection in Central America and the Pacific south of Mexico. Other cloud climatologies of deep convection (Garcia 1985), SAGE II, and MLS are all consistent in showing this decrease. Farther north, the effect is more profound, with substantially less high cloud and lower MLS water vapor overburdens around the Gulf of Mexico, over western Mexico, and in the central and south central US. All these indicators are consistent with a reduction in convective activity, as reflected in the reduced number of thunderstorms observed in the US during autumn (see the OTD Web Site, http://wwwghcc.msfc.nasa.gov/otd.html). Curiously, the HIRS high cloudiness in Hawaii is actually slightly greater than in the summer season. This is probably due to a weakening in the zonal asymmetry of the circulation with respect to the summer season, which implies weaker and less widespread downward motion in the mid-Pacific trough region. Both Figure 9*c* (summer) and Figure 9*d* (autumn) show an anticyclone over Mexico and Central America, with troughs over the adjacent Pacific and Atlantic oceanic regions. However, the pattern is substantially weaker during autumn.

4.3.5. Meteorological Summary

The picture that emerges from a detailed analysis of the SAGE II, HIRS, and MLS data in the context of our knowledge of cloud formation and atmospheric circulation is consistent and compelling. These satellite data clearly demonstrate that (1) the tropopause height, although important, is not the only factor in determining the frequency of clouds and the water vapor overburden above FL410, as some regions and seasons have substantially greater cloud cover in the very highest parts of the troposphere than others; and (2) these patterns are consistent with what is known about the upper tropospheric circulation and distribution of water vapor. Hence, these data can be used with confidence to perform a site survey for SOFIA.

5. COMPARISON OF HOME BASE SITES

5.1. Definition of Metrics

Since a multiyear airborne program (Larson 1992) requires observations of hundreds of objects and makes use of a wide

variety of flight tracks, any comparison of home base sites for SOFIA must consider the meteorological data in Figures 4, 5, 6, and 7 over extended regions. Experience with flight planning on the LJO and KAO suggests that some flight plans will be primarily north-south, while others will be primarily east-west. Some flight plans will include long legs that extend far from the home base, while other plans will include more objects, each being observed for a shorter time, and will tend to criss-cross back and forth over the home base. This suggests that the amount of time spent flying over each geographic location will be described by some type of near-Gaussian distribution centered on or near the home base. This premise is borne out by an analysis of 48 typical research flights aboard the KAO between 1993 and 1995 (A. W. Meyer, private communication). The air speed for SOFIA is ~8% larger than for the KAO, which suggests that its spatial distribution of flight tracks may extend over a slightly larger region.

Extrapolating the KAO experience to SOFIA, the spatial distribution of flight tracks is approximated by

$$S(x, y) = \exp\left(-\ln 2\{[(x - x_0)/a]^2 + [(y - y_0)/b]^2\}\right), \quad (16)$$

where $a = 650$ statute miles and $b = 275$ statute miles. The quantity $S(x, y)$ represents the relative amount of time spent flying over each geographic location x, y near the home base location x_0, y_0. The locus of points where $S = 0.5$ is an ellipse with semimajor and semiminor axes a and b, respectively. For comparison with Figures 4, 5, 6, 7, 8, 9, and 10, the major (east-west) axis of this ellipse roughly spans Utah, Colorado, Kansas, and Missouri, and the minor (north-south) axis nearly spans Colorado and New Mexico.

Using equation (16), the area-weighted frequency of cloud occurrence for each site is computed from

$$\langle f_X \rangle = \frac{\int_{-\infty}^{\infty}\int_{-\infty}^{\infty} S(x, y)\ f_X(x, y)\ dx\ dy}{\int_{-\infty}^{\infty}\int_{-\infty}^{\infty} S(x, y)\ dx\ dy}, \quad (17)$$

where $f_X(x, y)$ is either the spatial distribution of SAGE clouds, $f_{\rm SAGE}$, or the corresponding quantity from HIRS, $f_{\rm HIRS}$ (§§ 2.2 and 2.3, respectively). These two area-weighted metrics can be used to compare different sites but must be renormalized to be intercompared because their cutoff optical depths are very different (§ 2). Similarly, the area-weighted zenith water vapor overburdens are computed from

$$\langle z \rangle = \frac{\int_{-\infty}^{\infty}\int_{-\infty}^{\infty} S(x, y)\ z(x, y)\ dx\ dy}{\int_{-\infty}^{\infty}\int_{-\infty}^{\infty} S(x, y)\ dx\ dy}, \quad (18)$$

where $z(x, y)$ is taken from either equation (8) or equation (14). The results are the area-weighted water vapor overburdens, $\langle z' \rangle$ and $\langle z'' \rangle$, as estimated from the SAGE II/tropopause height and MLS data, respectively. Since the former is a clear-sky climatology and the latter includes cloudy days as well, these metrics will agree only for relatively cloud-free sites, and, more generally, $\langle z' \rangle$ will be less than $\langle z'' \rangle$. Unlike the case for a ground-based observatory, where only the weather directly overhead is of concern, the calculated metrics weight the high-altitude weather over an extended region (roughly $\pm 11°$ in longitude and $\pm 4°$ in latitude) because flight planning is a complex process that benefits from the ability to fly long distances in any direction.

5.2. Comparison of Metrics

Figures 4, 5, 6, and 7 contain the data required to evaluate the relative merits of any continental US site. As specific examples, we consider Moffett Field, CA; Seattle, WA; Tucson, AZ; Austin, TX; Minneapolis, MN; Miami, FL; and Washington, DC, in the continental US. In addition, Hickam Field, HI; Bonn, Germany; and Christchurch, New Zealand are included as possible deployment sites.

Table 2 shows a number of area-weighted, meteorological quantities at these sites for each season. The values of the metrics for the various sites are not strongly dependent on the half-widths of the flight distribution (a and b in eq. [16]). Three flight levels are included because the goal for SOFIA is to routinely provide quality observing times of at least 2.25 hr at FL410, 2.5 hr at FL430, and 1.25 hr at FL450 on a nominal 7.5 hr flight (Remmers 1996). The actual performance of SOFIA will depend on the 747-SP aircraft selected and the design of its mission systems. The metrics for cloud cover and water vapor overburden should be simultaneously minimized to best accommodate airborne observations.

The area-weighted tropopause pressure, $\langle P_T \rangle$, given in Table 2 is plotted in Figure 11 as a function of season. Consistent with the KAO experience, Moffett Field, CA, is found to have routine access to the stratosphere at FL410 in the winter and spring. During the other two seasons, operations at FL410 are near the tropopause and ascent to FL450 often penetrates into the stratosphere. To first order, tropopause height depends on latitude—Washington, DC, is the most similar in latitude to Moffett Field and has a very similar tropopause height versus season. The more southerly sites (Hickam Field, Miami, Austin, and Tucson) have area-weighted tropopause heights that are significantly higher than those for Moffett Field, and the more northerly sites (Minneapolis, Seattle, and Bonn) have lower values. In Christchurch, the only Southern Hemisphere site considered, the seasons are reversed, and the average tropopause height is generally low because of its high southern latitude.

The area-weighted SAGE II and HIRS frequency of cloud occurrence, $\langle f_{\rm SAGE} \rangle$ and $\langle f_{\rm HIRS} \rangle$, are plotted versus season for each site in Figures 12 and 13, respectively. Similarly, the area-weighted MLS-derived zenith water vapor overburden, $\langle z'' \rangle$, is plotted in Figure 14. The area-weighted zenith water vapor overburdens derived from the SAGE/tropopause height data, $\langle z' \rangle$, are not plotted as they represent a clear-sky climatology and do little to discriminate between sites (see Table 2). As expected, the cloud incidence and average overburdens in the

TABLE 2
METEOROLOGICAL CONDITIONS FOR AIRBORNE ASTRONOMY HOME BASE SITES

QUANTITY (Units)	FLIGHT LEVEL	WINTER SEASON (DJF)										SPRING SEASON (MAM)									
		HI	CA	WA	AZ	TX	MN	FL	DC	Ger	NZ	HI	CA	WA	AZ	TX	MN	FL	DC	Ger	NZ
SAGE clouds (%)	410	19.8	12.7	8.5	14.9	16.2	5.5	15.2	10.2	6.5	16.3	41.6	17.3	6.9	19.7	22.7	9.7	29.2	16.9	4.5	7.0
	430	15.4	6.3	3.8	8.7	10.4	2.1	10.5	4.9	3.0	6.7	35.7	8.9	2.5	12.9	15.9	4.4	23.0	9.6	2.2	3.1
	450	11.4	2.7	1.6	3.7	4.9	1.1	6.9	2.7	1.9	3.4	27.7	3.9	0.9	7.6	10.2	1.9	17.4	4.7	0.9	1.6
HIRS clouds (%)	410	1.7	3.0	3.1	3.6	4.5	2.7	3.2	3.7	1.7	1.2	2.5	2.4	1.6	4.1	7.3	2.4	4.3	3.4	1.0	2.0
	430	0.7	2.5	3.0	2.4	2.9	2.6	1.9	3.3	1.6	1.2	1.3	1.9	1.5	3.0	5.1	2.3	2.3	2.8	0.9	2.0
	450	0.7	2.0	2.1	2.3	2.9	1.9	1.8	2.5	1.1	0.8	1.3	1.4	1.0	2.9	5.0	1.6	2.2	2.1	0.6	1.6
$\langle P_T \rangle$ (mb)	...	103	207	246	178	154	257	110	215	237	193	115	198	239	169	152	229	120	203	245	208
$\langle z' \rangle$ burden (μm)	410	4.7	4.2	4.2	4.3	4.4	4.2	4.6	4.2	4.2	4.2	5.5	4.3	4.1	4.7	5.0	4.1	5.5	4.3	4.1	4.2
	430	3.8	3.8	3.8	3.8	3.8	3.8	3.8	3.8	3.8	3.8	4.2	3.8	3.8	3.9	4.0	3.8	4.2	3.8	3.8	3.8
	450	3.4	3.4	3.4	3.4	3.4	3.4	3.4	3.4	3.4	3.4	3.5	3.5	3.5	3.5	3.5	3.5	3.5	3.5	3.5	3.5
MLS (ppmv)	...	89	72	59	81	97	59	101	78	64	95	91	82	73	83	93	70	108	81	71	81
$\langle z'' \rangle$ burden (μm)	410	5.6	4.8	4.6	5.3	6.2	4.6	6.4	5.1	4.6	6.1	5.7	5.2	4.8	5.3	5.9	4.7	7.2	5.2	4.8	5.2
	430	4.5	4.2	4.1	4.3	4.8	4.1	4.9	4.3	4.1	4.7	4.5	4.3	4.2	4.3	4.6	4.1	5.2	4.3	4.1	4.3
	450	3.8	3.8	3.8	3.8	3.9	3.8	3.9	3.8	3.8	3.9	3.8	3.8	3.8	3.8	3.9	3.8	4.1	3.8	3.8	3.8

QUANTITY (Units)	FLIGHT LEVEL	SUMMER SEASON (JJA)										AUTUMN SEASON (SON)									
		HI	CA	WA	AZ	TX	MN	FL	DC	Ger	NZ	HI	CA	WA	AZ	TX	MN	FL	DC	Ger	NZ
SAGE clouds (%)	410	33.1	20.6	15.3	40.1	59.4	29.1	73.2	49.9	7.7	1.5	31.6	12.5	9.9	16.1	25.6	12.2	46.5	23.3	9.6	1.5
	430	23.9	12.4	8.1	32.9	52.6	20.2	67.9	41.6	4.0	0.4	29.0	6.8	4.7	11.8	21.7	7.4	41.6	16.7	3.8	0.0
	450	20.2	10.5	5.5	28.4	46.3	14.8	57.9	29.4	2.7	0.2	24.3	3.0	1.8	8.1	17.7	3.3	36.8	9.9	1.5	0.0
HIRS clouds (%)	410	2.8	0.8	1.9	4.5	7.2	3.2	8.9	3.4	2.1	3.7	3.8	1.5	2.3	2.4	3.9	2.7	5.4	2.2	1.6	2.0
	430	1.5	0.6	1.8	3.0	4.4	3.0	4.9	2.5	2.0	3.6	1.9	1.3	2.2	1.4	2.2	2.6	2.8	1.7	1.5	1.9
	450	1.5	0.4	1.2	2.7	4.1	2.2	4.6	1.7	1.5	2.9	1.9	1.0	1.6	1.3	2.1	1.9	2.6	1.2	1.1	1.5
$\langle P_T \rangle$ (mb)	...	121	150	205	126	124	174	123	148	219	252	115	158	205	134	128	209	119	165	218	250
$\langle z' \rangle$ burden (μm)	410	7.1	6.3	4.7	6.9	7.0	5.6	7.0	6.3	4.3	4.0	6.2	5.6	5.0	5.9	6.0	4.9	6.2	5.5	4.8	4.4
	430	5.6	5.1	4.0	5.5	5.6	4.6	5.6	5.1	3.8	3.7	5.0	4.7	4.3	4.9	4.9	4.3	5.0	4.6	4.2	4.0
	450	4.3	3.9	3.4	4.3	4.3	3.6	4.3	4.0	3.4	3.4	3.7	3.7	3.7	3.7	3.7	3.7	3.7	3.7	3.7	3.7
MLS (ppmv)	...	117	98	93	121	141	103	154	139	102	55	124	93	90	95	114	81	136	104	81	65
$\langle z'' \rangle$ burden (μm)	410	8.1	6.4	5.9	8.9	11.5	6.8	13.8	11.3	6.6	4.5	9.0	6.0	5.7	6.1	7.9	5.2	10.6	6.9	5.1	4.6
	430	5.7	4.8	4.6	6.2	7.6	5.0	8.8	7.4	4.9	4.1	6.2	4.6	4.5	4.7	5.6	4.3	7.1	5.1	4.3	4.1
	450	4.3	4.0	3.9	4.6	5.3	4.0	6.0	5.3	4.0	3.8	4.6	3.9	3.8	3.9	4.3	3.8	5.0	4.1	3.8	3.8

Northern Hemisphere are generally highest in the summer when the surface temperatures are greatest and the tropopause is highest. Consistent with the KAO experience, Hawaii has higher summertime cloud cover and water vapor overburdens than Moffett Field (KAO deployments to Hawaii occurred from May to September; ~3/4 were in the summer), and New Zealand has low cloud cover and water vapor overburdens in spring and autumn (KAO deployments were mainly in April–May, some were in November).

Table 2 and Figures 12–14 also show that, in summer, Miami has the highest area-weighted metric in all three indicators (SAGE, HIRS, and MLS) and that Austin, Washington, and Tucson are also worse than Hawaii during this season. On the other hand, Moffett Field, Seattle, Minneapolis, Bonn, and Christchurch have consistently better high-altitude summertime weather than Hawaii. The differences between sites are considerably smaller in winter and spring and are intermediate for autumn.

The average water vapor overburden on cloudy days can be estimated from inverting the expression

$$\langle z'' \rangle = \alpha \langle z' \rangle + (1 - \alpha) \langle z_{\text{cloudy}} \rangle , \tag{19}$$

where $\langle z'' \rangle$ is the average MLS (all days) overburden, $\langle z' \rangle$ is the average SAGE II/tropopause (clear-sky) overburden, and α is the fraction of the SAGE II profiles complete down to FL410. If the HIRS values in Table 2 are used in conjunction with Figure 1 to estimate α and $\langle z' \rangle$ and $\langle z'' \rangle$ are taken from Table 2, then equation (19) can be solved for the average cloudy-day overburden, $\langle z_{\text{cloudy}} \rangle$. The results are shown in Table 3; they range from 6 to 7 μm for Christchurch and Moffett Field to greater than 15 μm for Austin, Miami, and Washington. Since these are average values, even larger overburdens will be experienced on some days (see Fig. 2). For reference, the SOFIA Request For Proposal required that the zenith water vapor overburden not exceed 10 μm during routine science operations (Remmers 1996).

The frequencies of cloud occurrence presented in Table 2

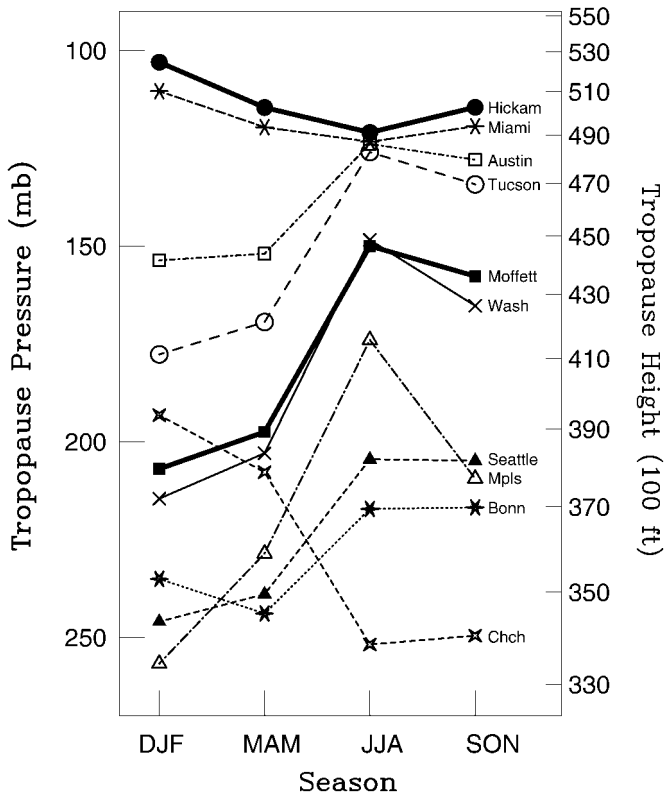

FIG. 11.—Area-weighted tropopause pressure (or height) for each site as a function of season.

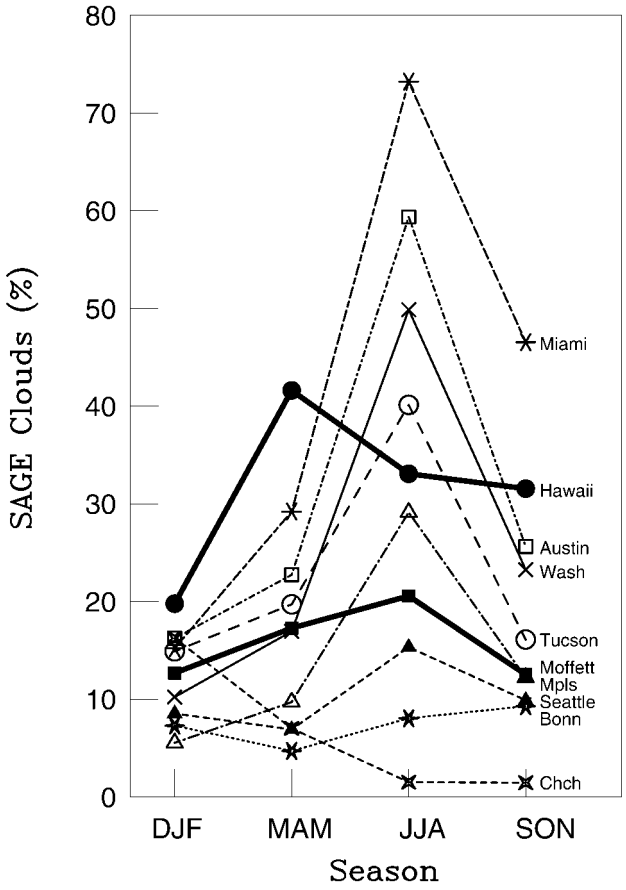

FIG. 12.—Area-weighted SAGE II frequency of cloud occurrence for each site as a function of season.

and Figures 12 and 13 are the area-weighted averages of the unnormalized satellite values introduced in § 2. Hence, the quantities $\langle f_{\rm SAGE}\rangle$ and $10\langle f_{\rm HIRS}\rangle$ are estimates of the fraction of flights that will encounter clouds and the quantities $\langle C_{\rm SAGE}\rangle = 0.2\langle f_{\rm SAGE}\rangle$ and $\langle C_{\rm HIRS}\rangle = 2\langle f_{\rm HIRS}\rangle$ are estimates of the fraction of total flight time which will be flown under clouds (see eqs. [5] and [6]). Even when so normalized, the SAGE II and HIRS data are independent and not always in agreement because of different measurement techniques and horizontal resolutions. Nonetheless, they indicate very similar weather patterns and show that meteorological conditions improve quickly with increasing altitude.

A qualitative feeling for these results can be obtained by studying the contours in Figures 4, 5, 6, and 7. These figures clearly show that the poorest high-altitude weather is southeast of a line which extends from Baja California to the mid-Atlantic states and includes all of the southern states and significant portions of the southwestern and lower midwestern states. Conversely, the region northwest of this line possesses meteorological conditions that are generally more favorable to airborne astronomy. The differences among the continental US sites are greatest in the summer. This is due to the contrast between the upward motion and convection in the south central US associated with the monsoon anticyclone, and the downward drying motion in the well-developed Pacific trough (see § 4). In the other seasons, the differences between sites diminish and are primarily controlled by local thunderstorm activity (spring) and the midlatitude storm tracks (winter).

6. DISCUSSION

This site survey uses the most comprehensive meteorological data presently available to ascertain the high-altitude weather conditions over the US and surrounding regions and to understand the implications of site location for the productivity of an airborne observatory. As discussed in § 4, there are many reasons to believe that these data are typical of the average meteorological conditions to be encountered at flight altitudes over the North American Region. As discussed in §§ 2 and 3, higher incidences of clouds and/or higher water vapor overburdens translate directly into reduced observing efficiency. Clouds not only increase sky noise, they can also obscure the visible stars used for guiding and attenuate the measured radiation in unpredictable ways, which makes it difficult to edit the data reliably. In cases in which clouds are encountered during setup or calibration legs, entire flights may be lost. The primary effect of increased water vapor overburdens on airborne observations is to reduce sensitivity, thereby increasing

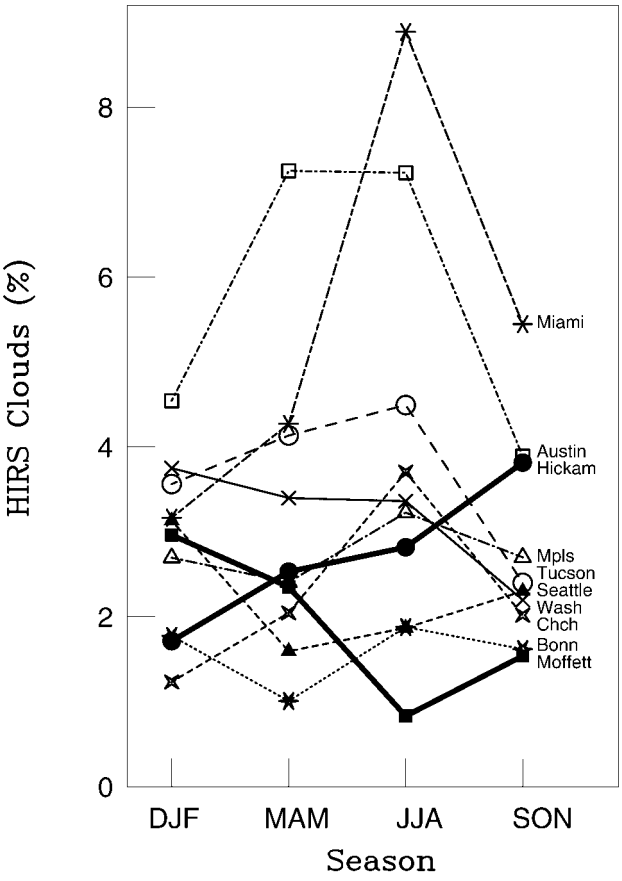

FIG. 13.—Area-weighted HIRS frequency of cloud occurrence for each site as a function of season.

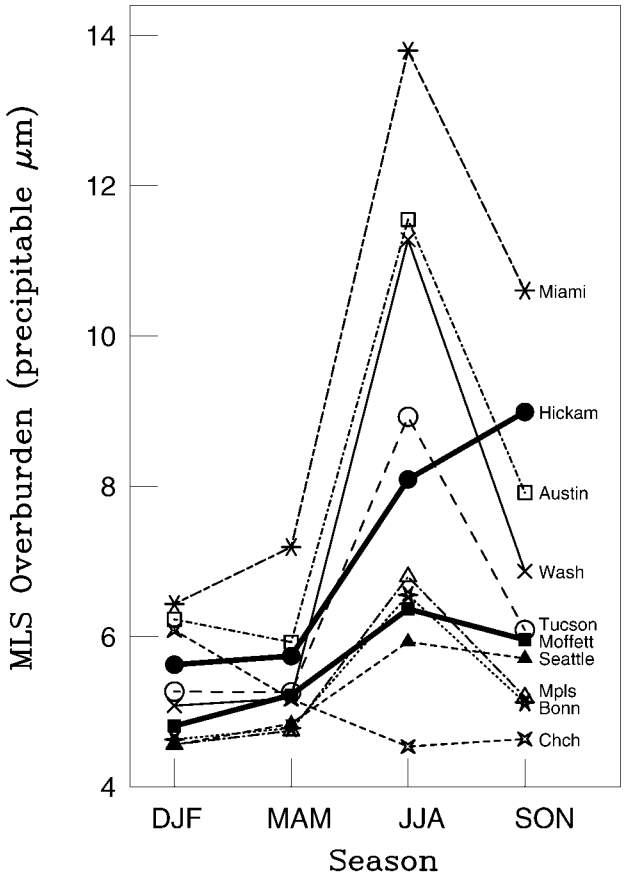

FIG. 14.—Area-weighted MLS-determined zenith water vapor overburden for each site as a function of season.

the time required for a given observation (Erickson 1998). Some investigations requiring the driest observing conditions will be ruled out at the wetter sites (e.g., the KAO observations of N II [122 μm] by Colgan et al. 1993). Just as the climb and loiter performance of SOFIA should be maximized by careful attention to aircraft selection, scientific payload weight, and drag produced by the open-port telescope cavity, so also should its home base be carefully selected to provide the best possible observing conditions.

Such considerations are particularly important for SOFIA because its 20°–60° elevation range is considerably lower than the 35°–75° range of the KAO. This means that the average observing elevation will also be lower, as the number of available objects increases with decreasing elevation. Hence, it will be important to minimize the zenith water vapor overburden for SOFIA to mitigate the effects of a larger average air mass than that experienced on the KAO. Similarly, SOFIA will have an environmental control system that will keep its mirrors much cleaner than those on the KAO, so more observations will be background limited by the sky, rather than by telescope emission. This means that SOFIA will be more sensitive to the presence of high-altitude, thin cirrus than was the KAO.

Over the past 21 yr (1424 research flights), the KAO typically found low to moderate water vapor overburdens and a relatively low incidence of high-altitude clouds at FL410 on flights based at Moffett Field, CA, and Christchurch, New Zealand. On the other hand, the KAO encountered larger water vapor overburdens and a higher frequency of high-altitude clouds in Hawaii (Meyer 1996). This experience prompted the SOFIA Science Working Group to declare at its 1996 February meeting that Hawaii would be unacceptable as a home base for SOFIA

TABLE 3
AVERAGE WATER VAPOR OVERBURDEN ON CLOUDY SUMMER DAYS

Geographic Site	α	$\langle z_{\rm cloudy} \rangle$ (precip. μm)
Hickam, HI	0.73	11
Moffett Field, CA	0.85	7
Seattle, WA	0.78	10
Tucson, AZ	0.63	12
Austin, TX	0.47	15
Minneapolis, MN	0.71	10
Miami, FL	0.37	18
Washington, DC	0.70	23
Bonn, Ger	0.77	14
Christchurch, NZ	0.68	6

operations; it was specifically excluded from consideration in the SOFIA Request For Proposal (Remmers 1996). The present analysis confirms that the regions surrounding Moffett Field, CA, and Christchurch, New Zealand, possess quite favorable conditions for airborne astronomy and corroborates the generally poorer observing conditions found on KAO summertime flights over Hawaii. Comparison of the meteorological conditions over the continental US finds large variations in the high-altitude cloud cover and water vapor overburdens and illustrates the importance of careful site selection for airborne astronomy.

The largest differences in high-altitude weather occur in the summertime because the sites are in very different meteorological regimes in terms of large-scale circulation and the potential for convection. The eastern Pacific is dominated by the downward motion associated with the mid-Pacific upper level trough and by generally cool sea surface temperatures. East of a line extending from northern Mexico along the Rockies into Canada, there is upward motion associated with the continental upper level ridge. Warm moist air from the Gulf of Mexico, and to a lesser extent the Gulf of California, promotes convection east of the Rockies and in northwestern Mexico. The Moffett Field and Seattle sites are well within the regime of downward motion and low upper level cloudiness, whereas Miami, Austin, and Washington are well within the regime of upward motion and high upper level cloudiness; Tucson and Minneapolis are near the boundary between these two regimes.

The authors wish to thank the many colleagues who patiently gave of their time to make this study possible, including R. Chatfield, E. Jensen, P. Pilewskie, and R. Selkirk (NASA-ARC) for many meteorologically useful conversations and references; J. Bregman, E. Erickson, E. Jensen, and R. Selkirk (NASA-ARC) for their comments on the manuscript; P. McCormick, G. Kent, P.-H. Wang, and K. Skeens (NASA-LaRC) for special processing of the SAGE II cloud data; D. Hartmann (University of Washington) for providing an electronic copy of the MLS data and B. Read (NASA-JPL) for assistance in interpreting it; D. Wylie for providing an electronic copy of the HIRS cloud data; A. Meyer (NASA-ARC) for archival research on the KAO experience; D. Wooden (NASA-ARC) and D. Dowell (University of Chicago) for helpful discussions on the impact of clouds on airborne observations; and S. Barrett (Ball Aerospace) and W. Chan (SJSU) for their programming support.

REFERENCES

Bader, M., & Wagoner, C. B. 1970, Appl. Opt., 9, 265
Barath, F., et al. 1993, J. Geophys. Res., 98, 10751
Baum, B. A., et al. 1995, J. Atmos. Sci., 52, 4210
Baum, B. A., Wielicki, B. A., & Minnis, P. 1992, J. Appl. Meteorol., 31, 351
Bottomley, M., Folland, C. K., Hsiung, J., Newell, R. E., & Parker, D. E. 1990, Global Ocean Surface Temperature Atlas, UK Meteorological Office and MIT Department of Earth and Planetary Science
Cameron, R. M., Bader, M., & Mobley, R. E. 1971, Appl. Opt., 10, 2011
Christian, H. J., Blakeslee, R. J., & Goodman, S. J. 1989, J. Geophys. Res., 94, 13329
Colgan, S. W. J., Haas, M. R., Erickson, E. F., Rubin, R. H., Simpson, J. P., & Russell, R. W. 1993, ApJ, 413, 237
Craig, R. A. 1965, The Upper Atmosphere: Meteorology and Physics (New York: Academic)
Danielsen, E. F. 1982, Geophys. Res. Lett., 9, 605
Danielsen, E. F., Gaines, S. E., & Hipskind, R. S. 1983, An Atlas of Objectively Analyzed Atmospheric Cross Sections 1973–1980, prepared for NASA-Ames Research Center under Cooperative Agreement NCC 2-73
Doherty, G. M., Newell, R. E., & Danielsen, E. F. 1984, J. Geophys. Res., 89, 1380
Douglas, M. W., Maddox, R. A., & Howard, K. 1993, J. Climate, 6, 1665
Emanuel, K. A. 1994, Atmospheric Convection (New York: Oxford Univ. Press)
Erasmus, D. A. 1986, PASP, 98, 254
Erickson, E. F. 1998, PASP, submitted
Erickson, E. F., & Davidson, J. A. 1995, in ASP Conf. Proc. 73, Airborne Astronomy Symposium on the Galactic Ecosystem: From Gas to Stars to Dust, ed. M. R. Haas, J. A. Davidson, & E. F. Erickson (San Francisco: ASP), 707
Erickson, E. F., Simpson, J. P., Kuhn, P. M., & Stearns, L. P. 1979, NASA TM78582
Garcia, O. 1985, Atlas of Highly Reflective Clouds for the Global Tropics: 1971–1983, US Department of Commerce, National Oceanic and Atmospheric Administration, and Environmental Research Laboratories (Washington, DC: GPO)
Gultepe, I., & Starr, D. O'C. 1995, J. Atmos. Sci., 52, 4159
Hall, F. F. 1968, Appl. Opt., 7, 891
Holton, J. R., and Colton, D. E. 1972, J. Atmos. Sci., 29, 1124
Houze, R. A. 1989, Q. J. R. Meterol. Soc., 115, 425
Jensen, E. J., Toon, O. B., Selkirk, H. B., Spinhirne, J. D., & Schoeberl, M. R. 1996, J. Geophys. Res., 101, 21361
Jin, Y., Rossow, W. B., & Wylie, D. P. 1996, J. Climate, 9, 2850
Johnson, R. H., Gallus, W. A., Jr., & Vescio, M. D. 1990, J. Atmos. Sci., 47, 2200
Kelly, K., Proffitt, M. H., Chan, K. R., Loewenstein, M., Podolske, J. R., Strahan, S. E., Wilson, J. C., & Kley, D. J. 1993, J. Geophys. Res., 98, 8713
Kent, G. S., Winker, D. M., Osborn, M. T., & Skeens, K. M. 1993, J. Geophys. Res., 98, 20725
Kent, G. S., Winker, D. M., Wang, P.-H., & Skeens, K. M. 1995, Bull. Am. Meteorol. Soc., 76, S67
Keyser, D., & Shapiro, M. A. 1986, Mon. Weather Rev., 114, 452
Krishnamurti, T. N. 1971, J. Appl. Meteorol., 10, 1066
Kuhn, P. M. 1982, Geophys. Res. Lett., 9, 621
Larsen, J. C., Chiou, E. W., Chu, W. P., McCormick, M. P., McMaster, L. R., Oltmans, S., & Rind, D. 1993, J. Geophys. Res., 98, 4897
Larson, H. P. 1992, PASP, 104, 146
Liao, X., Rossow, W. B., & Rind, D. 1995, J. Geophys. Res., 100, 1121
Lilly, D. K., Waco, D. E., & Adelfang, S. I. 1974, J. Appl. Meteorol., 13, 488
Lord, S. D., Hollenbach, D. J., Haas, M. R., Rubin, R. H., Colgan, S. W. J., & Erickson, E. F. 1996, ApJ, 465, 703
Mace, G. G., Starr, D. O'C., Ackerman, T. P., & Minnis, P. 1995, J. Atmos. Sci., 52, 4094
McCormick, M. P. 1987, Adv. Space Res., 7, (3)219

McCormick, M. P., Edwards, H. B., Maudin, L. E., III, & McMaster, L. R. 1976, NASA Rep. CP2004
McCormick, M. P., Hamill, P., Pejin, T. J., Chu, W. P., Swissler, T. J., & McMaster, L. R. 1979, Bull. Am. Meteorol. Soc., 60, 1038
Menzel, W. P., Wylie, D. P., & Strabala, K. I. 1992, J. Appl. Meteorol., 31, 370
Meyer, A. W. 1996, SOFIA Engineering Report SER-AWM-002
Morrison, D., Murphy, R. E., Cruikshank, D. P., Sinton, W. M., & Martin, T. Z. 1973, PASP, 85, 255
Newell, R. E., Kidson, J. W., Vincent, D. G., & Boer, G. J. 1973, The General Circulation of the Tropical Atmosphere and Interactions with Extratropical Latitudes, Vol. 1 (Cambridge, Mass: MIT Press)
Newell, R. E., Zhu, Y., Browell, E. V., Ismail, S., Read, W. G., Waters, J. W., Kelly, K. K., & Liu, S. C. 1996, J. Geophys. Res., 101, 1931
Nolt, I. G., Radostitz, J. V., Donnelly, R. J., & Stearns, L. P. 1979, NOAA Technical Report ERL 406-APCL 44
Nolt, I. G., & Stearns, L. P. 1980, in Atmospheric Water Vapor, ed. A. Deepak, T. D. Wilkerson, & L. H. Ruhnke (New York: Academic), 343
Oort, A. H., & Rasmusson, E. M. 1970, Mon. Weather Rev., 98, 423
Palmén, E., & Newton, C. W. 1969, Atmospheric Circulation Systems (New York: Academic)
Platt, C. M. R. 1979, J. Appl. Meteorol., 18, 1130
Platt, C. M. R., Spinhirne, J. D., & Hart, W. D. 1989, J. Geophys. Res., 94, 11151
Prabhakara, C., Kratz, D. P., Yoo, Y.-M., Dalu, G., & Vernekar, A. 1993, J. Quant. Spectrosc. Radiat. Transfer, 49, 467
Read, W. G., Waters, J. W., Flower, D. A., Froidevaux, L., Jarnot, R. F., Hartmann, D. L., Harwood, R. S., & Rood, R. B. 1995, Bull. Am. Meteorol. Soc., 76, 2381
Reber, C. A., Trevathan, C. E., McNeal, R. J., & Luther, M. R. 1993, J. Geophys. Res., 98, 10643
Remmers, H. W. 1996, SOFIA Request For Proposal, RFP2-36267(HWR), issued April 26 by NASA-Ames Research Center
Rind, D., Chiou, E.-W., Chu, W., Oltmans, S., Lerner, J., Larsen, J., McCormack, M. P., & McMaster, L. 1993, J. Geophys. Res., 98, 4835
Russell, J. M., III, et al. 1993, J. Geophys. Res., 98, 10777
Schiffer, R. A., & Rossow, W. B. 1983, Bull. Am. Meteorol. Soc., 64, 779
Schubert, S. D., Rood, R. B., & Pfaendtner, J. 1993, Bull. Am. Meteorol. Soc., 74, 2331
Soden, B., & Bretherton, F. P. 1993, J. Geophys. Res., 98, 16669
Spinhirne, J. D., & Hart, W. D. 1990, Mon. Weather Rev., 118, 2329
Starr, D. O'C., & Wylie, D. P. 1990, Mon. Weather Rev., 118, 2259
Tarrius, A., Papoular, R., & Lebertre, T. 1982, in Proc. 2nd ESO Infrared Workshop, The Struggle against Sky Noise in Ground-based and Airborne Observations (Garching, ESO)
Tsuda, T., Murayama, Y., Wiryosumarto, H., Harijono, S. W. B., & Kato, S. 1994, J. Geophys. Res., 99, 10491
Udelhofen, P., & Hartmann, D. 1995, J. Geophys. Res., 100, 7423
US Standard Atmosphere. 1962, NASA, USAF, and US Weather Bureau (Washington, D.C.: GPO)
Uttal, T., Clothiaux, E. E., Ackerman, T. P., Intrieri, J. M., & Eberhard, W. L. 1995, J. Atmos. Sci., 52, 4276
Wang, P.-H., Minnis, P., McCormick, M. P., Kent, G. S., & Skeens, K. M. 1996, J. Geophys. Res., 101, 29407
Warren, S. G., Hahn, C. J., London, J., Chervin, R. M., & Jenne, R. L. 1986, Global Distribution of Total Cloud Cover and Cloud Type Amounts over Land, US Department of Energy and National Center for Atmospheric Research, DOE/ER/60085-H1 and NCAR Technical Note NCAR/TN-273+STR
Waters, J. W., Froidevaux, L., Read, W. G., Manney, G. L., Elson, L. S., Flower, D. A., Jarnot, R. F., & Harwood, R. S. 1993, Nature, 362, 597
Webster, P. J. 1972, Mon. Weather Rev., 7, 518
Westphal, J., Neugebauer, G., & Leighton, R. B. 1974, Final Report for NASA Grant NGR 05-002-184, Infrared Sky Noise Survey, NASA-CR-139693 (N74-32782)
White, G. H. 1982, J. Atmos. Sci., 39, 24
Wijnbergen, J. J., Léna, P., & Celnikier, L. M. 1978, Infrared Phys., 18, 157
Winker, D. M., & Vaughan, M. A. 1994, Atmos. Res., 34, 117
Wylie, D. P., & Menzel, W. P. 1989, J. Climate, 2, 380
Wylie, D. P., Menzel, W. P., Woolf, H. M., & Strabala, K. I. 1994, J. Climate, 7, 1972
Wylie, D., Piironen, P., Wolf, W., & Eloranta, E. 1995, J. Atmos. Sci., 52, 4327